Magma imaged magnetotellurically beneath an active and an inactive magmatic segment in Afar, Ethiopia

Magma imaged magnetotellurically beneath an active and an inactive magmatic segment in Afar, Ethiopia

N E Johnson[1,2], K A Whaler[1], S Hautot[3], S Fisseha[4], M Desissa[1,5] and GJK Dawes[1]

[1]School of GeoSciences, University of Edinburgh, James Hutton Road, Edinburgh, EH9 3FE
[2]now at Stag Energy, 49 York Place Edinburgh EH1 3JD
[3]Imagir, 38 rue Jim Sévellec, Technopôle Brest-Iroise, 29200 Brest, France
[4]Institute of Geophysics, Space Sciences and Astronomy, Addis Ababa University, Addis Ababa, Ethiopia
[5]now at Geological Survey of Ireland, Beggars Bush, Haddington Road, Dublin 4, Ireland

Abstract

We present broadband magnetotelluric data collected along profiles over two magmatic segments comprising part of the sub-aerial Red Sea arm of the Afar triple junction, one active since late 2005, the other currently inactive. After robust processing and galvanic distortion analysis, we find the data pass the two-dimensional sub-surface resistivity modelling criteria. Profiles across the segments have well-defined geoelectrical strike directions parallel to the local rift axes. Data from the northern end of the active segment have a more ambiguous strike that is oblique to the profile and rift axis, but the direction does not have a severe impact on the model deduced. All three models display prominent zones of low resistivity, interpreted as arising from magma and partial melt. Petrological information has been used to constrain the resistivity of the parent melt, and hence to estimate melt fractions from the bulk resistivities. The total amount of melt estimated beneath the profile crossing the active segment, ~500 km^3, is approximately an order of magnitude greater than that beneath the profile crossing the currently inactive rift. This implies that magma availability is at least one factor affecting whether a segment is active.

1. Introduction

As part of a multi-disciplinary collaboration, we have collected broadband magnetotelluric (MT) data along three main profiles in the Afar region of Ethiopia, where the final stages of continental break-up are occurring (e.g. Wright et al., 2006). The tectonic setting of our study area is shown in Figure 1, and the area itself in Figure 2. Afar is the site of a rift-rift-rift triple junction where the Red Sea, Gulf of Aden, and Main Ethiopian rift (the northern-most part of the East African rift system) arms meet. It is separated from the Main Ethiopian rift by the Tendaho-Goba'ad discontinuity, accommodating the different spreading directions and rates through oblique slip (e.g. Ebinger et al., 2010). Extension in Afar is taking place primarily by dyke intrusion along pre-existing zones of crustal weakness, rather than by faulting, much as happens at mid-ocean ridges. It is localised into ~60 km long Quaternary magmatic segments that are similar in size, morphology, structure, and spacing to slow-spreading mid-oceanic ridge segments, and which cycle through periods of activity lasting typically a decade or so and then much longer periods of quiescence

(e.g. Hayward and Ebinger, 1996). The segments are heavily faulted over zones of ~20 km width (Rowland et al., 2007).

The main focus of the integrated study is the active Dabbahu magmatic segment, part of the sub-aerial Red Sea rift, on which the recent phase of rifting began in September 2005, when the whole ~60 km long segment was active as a dyke intruded ~2.5 km^3 of magma over a 2 week period, with up to 10 m of horizontal opening (Wright et al., 2006; Grandin et al., 2010). This occurred in a complicated spatio-temporal pattern from at least three sources, two near the Dabbahu and Gab'ho volcanoes at the northern end of the segment, the other near the Ado'Ale Volcanic Complex (AVC) towards its centre (Ayele et al., 2009). Magma intrusion continued for at least 3 months after this main event, and the associated subsidence and seismicity suggested a deflating magma chamber beneath Dabbahu volcano (Ebinger et al., 2008). Another 13 further dykes initiating near the AVC have re-intruded the central and southern section of the segment with a further ~0.5 km^3 of magma, gradually relieving the tectonic stress in regions of the segment associated with less opening in previous intrusions (Hamling et al., 2009). GPS and InSAR data show no surface displacement at the AVC associated with these dykes, except for minor subsidence following the 8^{th} in the sequence (Hamling et al., 2009). This suggests either a deep source, or that the magma chamber volume is maintained by degassing as intrusion occurs, or that it has large stiffness (Keir et al., 2009). Analysis of basaltic lavas from axial volcanoes indicates that melting occurs at 75-100 km depth; melt ascends rapidly, with brief storage at 5-7.5 km (Ferguson et al., 2010, 2013). Migrating earthquake swarms associated with intrusion have been used to infer magma moving from a depth of ~8 km (Ebinger et al., 2008, 2010; Belachew et al., 2011).

Geochemical and petrological analyses were also carried out on suites of older eruptive products, collected at the Dabbahu volcano (Field et al., 2012), one of two near the northern end of the segment, and the Badi volcano, about 25 km to the west of the rift axis and slightly to the north of the AVC (Ferguson et al., 2013). The ≤ 100,000 year old Dabbahu volcano has an erupted volume of >115 km^3 with a wide range of magma types (Field et al., 2013). Samples from the Badi area show magmatism has been occurring there for > 200,000 years (Lahitte et al., 2003), but it is dormant. Badi lavas have equilibrated near the top of the mantle before being transported to the surface, implying long-lived sub-crustal storage (Ferguson et al., 2013).

The MT method provides information on the electrical resistivity (or equivalently its inverse, electrical conductivity) of the sub-surface (e.g. Simpson and Bahr, 2005). There have been many MT studies of magmatic and rifting systems, both on land and in the marine environment. It has been used to investigate the plumbing system of and to monitor individual volcanoes, in both subduction zone and rift environments, including more recently identifying temporal changes in the data possibly arising from de-gassing (e.g. Aizawa et al., 2011). It is frequently employed in the exploration of hydrothermal/geothermal systems, including in identifying targets for geothermal power exploitation (see the review by Munoz, 2014). It has also proved invaluable in imaging the structure of and understanding the processes involved in magmatic systems, including the effects of mantle plumes (e.g. Wannamaker et al., 2008; Brasse

and Eydam, 2008; Bologna et al., 2011; Kelbert et al., 2012). Examples of rifting studies include those of Hautot et al. (2000), Simpson (2000) and Häuserer and Junge (2011) further south in the East African rift, Beneath mid-ocean ridges, MT has contributed to understanding mantle dynamics and the processes of melt generation (e.g. Baba et al., 2006; Key et al., 2013). Our study, of a slow spreading (Fig. 1) sub-ariel rifting area, has its closest analogy in the slow-spreading mid-Atlantic ridge, where magma chambers have been identified in the crust (MacGregor et al., 1998; Heinson et al., 2000), and Iceland (e.g. Miensopust et al., 2014). The aim of our MT studies was to image magma in the sub-surface, as an aid to understanding the processes involved in dyke intrusion and late-stage continental crustal extension. MT is ideally suited to this, for two main reasons. First, magma and partial melt have low electrical resistivity, typically orders of magnitude lower than that of their host rock, providing a good resistivity contrast. Second, MT is more sensitive to low resistivity than high resistivity material. One of our MT profiles, about 50 km long, crossed the axis of the Dabbahu magmatic segment, just to the north of the AVC. For comparison, we also collected data along a ~45 km long profile across the adjacent currently inactive Hararo segment to the south. We refer to these as the Dabbahu and Hararo profiles, respectively. The third profile passed to the west of the Dabbahu volcano at the northern end of the Dabbahu segment, and was oblique to the rift axis of the magmatic segment; this is known as the Teru profile, since it runs close to the village of Teru. It was 22.5 km long, with a slightly coarser site spacing than the other two. The locations of the sites making up the three profiles are shown on Figure 2, along with those of the volcanic and eruptive centres providing petrological information on magma composition used to constrain its resistivity.

Desissa et al. (2013; hereafter Paper 1) modelled the Dabbahu profile data and found low resistivities consistent with large quantities of partial melt, both in the crust and underlying mantle. These MT data were collected 2 months after the intrusion of the 8th dyke in the sequence and another 2 months before the 9th. The model has a mid-crustal conductor beneath the rift axis, with its top surface at about 5 km, but minimum resistivity in the range 10-15 km. Conservative estimates of melt volumes contained within it (Paper 1) are 25 km^3, an order of magnitude larger than the amount injected in the current rifting episode. Thus although its depth is consistent with the inferred dyke source, its large volume is inconsistent with only short-term storage. The model has a more extensive, Moho-straddling conductor to the west of the rifted zone, where the Badi volcano projects onto the profile, containing ~500 km^3 of melt. This deeper conductor is a good candidate to represent the long-term sub-crustal magma storage required to satisfy the geochemical data (Ferguson et al., 2013).

In section 2, we describe the data acquisition and processing, which leads to the conclusion that the data along each of the three profiles are broadly consistent with a two-dimensional (2D) sub-surface resistivity distribution. The 2D models for each of the profiles are compared in section 3, and we discuss their interpretation in section 4. Our conclusions are summarised in section 5.

2. The magnetotelluric method

The MT method is a passive source geophysical technique which involves measuring the time-varying horizontal components of electromagnetic fields induced in the sub-

surface by the changing external magnetic field. Details of the method and associated practicalities are given in text books such as Simpson and Bahr (2005) and Chave and Jones (2012). The electric field was determined from the voltages and distances (approximately 100m) between pairs of non-polarisable Pb-PbCl electrodes accurately orientated in the magnetic North-South and East-West directions, and the magnetic field measured by Metronix MFS05 or MFS06 broad-band induction coils, again accurately orientated North-South and East-West and precisely levelled. The electrodes were buried in a salty bentonite mud mixture to maintain good electrical contact with the earth in the arid environment of Afar, and the coils were buried to reduce wind noise. The sensors were connected to a pre-amplifier, and the data then transferred to a digitising and recording unit which also allowed real-time data quality control checks and preliminary processing to be performed, comprising a SPAM Mk3 (Ritter et al, 1998) or Mk 4 system. The equipment usually recorded for 1-2 days at each site. At most sites, we also deployed transient electromagnetic (TEM) equipment which monitors the resistivity of the very shallow sub-surface with a controlled source, keeping the MT and TEM centres co-located as closely as possible to ensure the two methods are probing the same lithologies. We used a Geonics PROTEM system with source loop of 100×100 m (similar to the MT electrode separation) and effective receiver loop size of 31.4 m^2. The time rate of decay of magnetic flux was recorded over integration times from 0.25 to 120 s. The majority of our sites were accessed by four-wheel drive vehicles, but those over and to the east of the rifted zone on the Dabbahu profile were installed using a helicopter owing to the rugged topography. Much of the surface cover in the region is competent rock and therefore unsuitable for burying coils and electrodes, but from SPOT satellite imagery we were able to identify suitable sites in advance, with patches of shallow sand and/or sedimentary cover of ~100m diameter or more, and away from rapid changes in topography as far as possible.

The MT data were robustly processed in the frequency domain using the algorithm of Chave and Thomson (1989) to obtain the so-called 'impedance tensor' embodying the sub-surface resistivity information. Short period ($<7.8 \times 10^{-3}$ s) data collected with the Metronix MFS05 induction coils were noisy, and have been excluded, but good quality data up to 1.2×10^{-4} s period are available at many sites on the Hararo and Teru profiles. At some sites the longest periods recoverable were only of order 100 s, but at many sites we have impedance tensor estimates at periods longer than 1000 s. We assessed whether the data along each profile were compatible with a 2D Earth using the 'strike' algorithm of McNeice and Jones (2001). This solves simultaneously for the geoelectrical strike direction (constant for all sites and periods), and parameters characterising the effect of small-scale shallow heterogeneities which cause non-inductive, or galvanic, effects in the data, also known as distortion, based on Groom-Bailey (GB) decomposition of the impedance tensor (Groom and Bailey, 1989).

The system of equations used to determine the distortion model parameters and geoelectrical strike direction is underdetermined, but can be fully resolved from the TEM data. The 'static shift' manifests itself as a period-independent vertical offset between the TE and TM mode apparent resistivity (the square of the relevant impedance tensor element amplitude). The curves should coincide at periods shorter than those penetrating the distorting region; however, even if they do, both may both be shifted by an equal amount. Failure to correct for static shift will lead to erroneous

models. Sternberg et al. (1988) show how suitably scaled TEM decay curves can be overlain on apparent resistivity curves to resolve static shift, since the two should coincide in their region of overlap. Examples from this study are shown in Figure 3, indicating that although often successful (Figure 3(a)), including identifying a static shift even though both mode apparent resistivities agree at short period (Figure 3(b)), on other occasions either there is insufficient period overlap to allow a static shift to be determined reliably (Figure 3(c)) or the two cannot be brought into agreement (Figure 3(d)). Site 812 in Fig 3(d) may be exhibiting distortion due to high electrode contact resistance (e.g. Ferguson, 2012).

The goodness-of-fit of the data to the distortion model indicates whether the 2D assumption is adequate. Misfits with the optimum strike direction for the three profiles considered here (Figure 2) are given in Table 1 and Figure S2 of Paper 1, both overall and for each site along the profile. There are some subtle trends in preferred strike as a function of period (and hence depth), which probably indicate a number of tectonic influences on the sub-surface structure, and possibly anisotropy effects. However, at most sites and periods, the misfit is below the value of 2 usually taken as indicating an acceptable fit to a 2D model.

Over a 2D Earth when the coordinate system is aligned with the geoelectric strike, only the off-diagonal impedance tensor elements are non-zero; they define two independent modes of induction known as the transverse electric (TE) and transverse magnetic (TM) modes, corresponding to electric currents flowing parallel and perpendicular to geoelectrical strike, respectively. The user must assign the impedance tensor elements to either the TE or TM mode, using geological or other information, since there is a 90° ambiguity. It is also useful to ascertain how well the strike direction is determined (for example, whether the distortion model fit is significantly worse for other assumed strike directions). The geoelectrical strike values quoted below, and the broad consistency with two-dimensionality, are based on the 'strike' algorithm, but were investigated by other methods, including phase tensor analysis (Caldwell et al., 2004), which is useful since the phase tensor is unaffected by static shift, GB decomposition applied to each site and period individually, and subsets of the data along each profile simultaneously, and the general decomposition technique of Counil *et al.*(1986). The geoelectrical strike for the Dabbahu profile is 340°, consistent with the strike of the rift axis; likewise, the Hararo profile strike of 330° also matches the slightly more westerly orientation of that segment axis (in both cases, the alternative perpendicular strike direction was ruled out on geological grounds). Thus both cross-rift profiles are essentially perpendicular to strike, the optimum arrangement for 2D modelling, with structure assumed invariant in the along-strike direction. For the Teru profile, the best-fitting strike directions are 316° or 046°, and thus the profile is not optimally orientated. We assumed a direction of 316°, closest to the rift axis orientation. However, the geoelectrical strike angle for this profile is considerably less well-defined. For the three most northerly sites, the data curves for the two modes at each site are very similar, and rotation has little effect on the size of the diagonal impedance tensor elements (i.e. the strike is undefined) or the fit to the distortion model. Also, for this profile only, different methods for determining strike angle give rather different values.

Finally, we used the ρ^+ algorithm (Parker and Booker, 1996) to perform a consistency check on the distortion- (including static shift-) corrected data assigned to their TE

and TM modes, as recommended by Jones and Ferguson (2001). The resulting Hararo mid-segment and Teru profile data are shown in Figures 4 and 5 respectively; those for the Dabbahu mid-segment profile were shown in Paper 1 (Figure 2). They are presented as pseudo-sections of apparent resistivity and phase (lag between electric and magnetic fields) as a function of period, which acts as a depth proxy. Apparent resistivity increases or decreases with period as sub-surface resistivity increases or decreases with depth, and phase less or greater than 45° indicates resistivity increasing or decreasing with depth, respectively; the phase responds to resistivity changes with depth at shorter periods than apparent resistivity. Thus both apparent resistivity and phase data for the profiles crossing the magmatic segments indicate two conductive zones in the sub-surface. The apparent resistivity lows are most prominent at periods of about 0.1-1s and then 100-1000s. The low, decreasing phases at the longest periods show the data detect a base to the deeper conductor. The dominant feature of the Teru profile apparent resistivities is the extensive zone of very low values (minimum 0.82 Ωm) at the northern end of the profile, close to the Dabbahu volcano, starting from periods of about 0.1s. This severely restricts the depth to which the data sample, although again the phase decrease with period at the longest periods suggests the base of this conductor is sensed. In the next section, modelling with 2D inversion confirms these deductions, and enables more quantitative inferences on the sub-surface resistivity distribution to be made.

3. Modelling

For 2D modelling, we use the rebocc algorithm of Siripunvaraporn and Egbert (2000), a regularised inversion approach which minimises a combination of the misfit between the data and their predictions by the model and a measure of the amount of structure in the model. Misfit is calculated in a weighted root-mean-square (RMS) sense, i.e. the expected value is 1. However, values significantly above 1 may still be regarded as an adequate fit, to allow for 3D and non-inductive effects in the data. Inversion is usually undertaken with a specified data error floor. The error floor can be different for the apparent resistivities and phases, recognising that static shift only affects apparent resistivity, or for the TE and TM modes, since the TM mode is less susceptible to 3D effects when, as here, it is expected to be associated with conductive features. We used an error floor of 10% throughout; altering it has little effect on the models obtained or the data predictions, though the RMS misfits change because of the re-scaling of error bars. The model space, parameterised into blocks of constant resistivity, is much larger than the area beneath the profiles, and extends to depths well beyond the penetration of the data, to allow the boundary conditions appropriate for this diffusion problem to be satisfied, using guidelines formulated by Weaver (1994). The first layer was 10 m thick, and layer thicknesses increased by a factor 1.2-1.5 to give a total model depth of about 130 km. The cells were typically 500 m wide beneath and just beyond the edges of the profile for the Dabbahu and Hararo profiles, and 1 km for the Teru profile where the site spacing was larger. We present the models to a depth of 35 km for the cross-rift profiles (slightly less than the resolution depth of about 40 km for the Dabbahu profile inferred from sensitivity tests in Paper 1), and 20 km for the shorter Teru profile where the very low resistivity at the northern end restricts the penetration of the data. The models are shown in Figure 6, and the data fits on a site-by-site basis in Figures 7, 8 and 10.

Despite the data providing a good fit to 2D distortion models, it is impossible to find 2D models adequately fitting some aspects of the data. Particular difficulties are presented by large changes in longer period TE mode apparent resistivities over short distances, most notably on the Dabbahu profile, and to a lesser extent between sites 915, 916 and 917, and between 907 and 110, on the Hararo profile (Figure 7), which are inconsistent with the 2D assumption. After excluding some data inconsistent with the 2D assumption and some particularly noisy data (as discussed in the Supplementary Material of Paper 1), the resulting best-fitting Dabbahu profile model has an RMS misfit of 2.3; that for the Hararo profile was 2.4. Most of the gross features of the data are well modelled, for instance, the data curves for the two modes separate at the right period, the magnitude of the split in the phases between the two modes is reasonably well-reproduced at most sites, and the TM mode predictions are usually good. The Teru profile model suffers less from these modelling issues, since the TE mode apparent resistivity at longer periods varies slowly and consistently along the profile, although it is slightly under-predicted at site 101 (Figure 8), which contributes most to the overall RMS misfit of 1.7. The Teru profile sites have progressively lower apparent resistivities at the longest periods moving north along the profile, which are well-matched by progressively lower model resistivities (reaching a minimum of 0.08 Ωm, considerably less than that of seawater at average salinity and temperature) over a greater vertical extent. However, the rapid drop in phase at the longest periods is not well reproduced, especially in the TM mode. This is most likely because regularised inversion tends to discriminate against the rapid increase in resistivity with depth it implies. There is also a hint of this in the TM mode apparent resistivities since the data curves level out or even have a slight upturn at the longest periods (Figure 8). The resistivity structure of the southern-most end of the model is similar to that of the Dabbahu profile model where the Teru profile projects on to it.

All three models have a thin, variable thickness (500m to 2 km) conducting layer close to, and sometimes reaching, the surface, embedded within otherwise resistive material, generally approaching 1000 Ωm, though typically an order of magnitude lower to the east of the rift axis on the Dabbahu profile. The high resistivity unit is likely to represent basaltic crust, whereas the conductive layer can be explained by large volumes of saline fluids/evaporite in recent sediments that have been extensively faulted, fractured and intruded, or highly weathered basalt (found at shallow depths in boreholes drilled for ground water). Field et al. (2012) find evidence for fractionation in the presence of brines in samples collected from the Dabbahu volcano and the AVC.There are large, economic salt deposits at Afdera and Dallol, to the north of Dabbahu, which Talbot (2008), Chernet (2012) and Atnafu et al. (2015) suggest result from repeated marine flooding (but see Hovland et al. (2008), who argue for a largely hydrothermal origin). Delays in crustal receiver functions across the area are consistent with substantial thicknesses of sediments (Hammond et al., 2011). At Dubti, to the south of the Hararo profile, boreholes found up to 1500m of lacustrine sediments (Abbate et al., 1995), or sediments interspersed with fissure basalts (Battistelli et al., 2002) as modelled by Bridges et al. (2012) to satisfy gravity and magnetic data.

Resistivity is significantly reduced in parts of the lower crust in the cross-rift profiles, whose base is ~ 22 km beneath the Dabbahu segment, and less well constrained at about 22-26 km beneath the Hararo segment (Hammond et al., 2011). This strongly

suggests the presence of substantial amounts of partial melt. The Dabbahu profile model has two distinct lower crustal conductors, one centred on the rift axis, the other with a deeper (~ 10 km) top surface extending into the mantle to the west of the rift axis, where the Badi volcano projects from a few kilometres north onto the profile. The Hararo profile has a single conductivity maximum in the lower crust, about 15 km to the east of the rift axis (which is at site 913) and at a depth of about 20 km, but the maximum is less pronounced compared to those on the Dabbahu profile and the whole of the lower crust is conductive.

The most striking feature of the Teru profile model is the extremely low resistivities inferred in the crust near the Dabbahu volcano (the white region in Figure 6, where $\log_{10}\rho < 0.1$ or $\rho < 1.26$ Ωm). Note that this feature is relatively unaffected by the choice of geoelectrical strike direction assumed – in fact, the model beneath the most northerly three sites is very similar in the extreme case of a 90° change to assumed geoelectrical strike angle (i.e. when the TE and TM modes are swapped). Since regularised inversion tends to smear structure, especially vertically, and discriminate against rapid changes in resistivity, it is difficult to be precise about the vertical variations in resistivity, apart from the depth to the top surface of the conductor. The data sense a decrease in resistivity at the longest periods, so it is not plausible to distribute the conductive material over greater depths than in the model of Figure 6. Forcing a resistive (1000 Ωm) mantle (starting at ~22 km depth, the crustal thickness there; Hammond et al, 2011) slightly reduces the data misfit, primarily by fitting the longest period data at sites 102-104 better. The model is unphysical – it has a conductive zone (minimum resistivity of only 0.03 Ωm) beginning at about 3 km depth beneath site 104, broadening to ~10 km wide with depth, terminating abruptly at the Moho, which would be an implausible melt distribution. However, it does suggest that a model with a more rapid depth termination of the conductor than is obtained by unconstrained regularised inversion would be more appropriate. The conductance also depends on the resistivity structure, with a maximum of 98 kS, equivalent to about 20 km of seawater, for the model of Figure 6, but 265 kS when the conductor is confined to the crust. The high conductivities encountered and relatively short profile mean that depth resolution is limited, so although the data sense some deeper structure, its nature is extremely uncertain; we therefore limit the depth extent to which this profile is displayed in Figure 6 to 20 km, but caution that the details of the structure shown even towards the base of the crust are ambiguous. Similarly, the structure to the north of site 104 is poorly constrained owing to the absence of sites there.

4. Interpretation

The 2D resistivity models can be used to infer minimum amounts of magma in the sub-surface. The low resistivity values indicate well-connected melt, implying that the parallel conducting pathways (Roberts and Tyburczy, 1999) or Hashin-Shtrikman upper bound (Hashin and Shtrikman, 1962) model is appropriate to infer melt fractions from bulk resistivity. For both models, the result depends only on melt fraction and melt resistivity, being virtually insensitive to host rock resistivity. Minimum melt percentages derived here are obtained from the parallel pathways model, in which current flows parallel to sheets of either melt or solid whose relative thicknesses are given by the volume fraction. The lower crustal basaltic melt resistivity estimated from geochemical analysis of samples from Dabbahu, Badi and

the AVC (Field et al., 2012; Ferguson et al., 2013) at ~20 km depth using the web-based tool Sigmelts (Pommier and Le Trong, 2011) was 0.28 Ωm (Paper 1). In Paper 1, we noted that given the range of geochemical uncertainties, SiO_2 content has the biggest influence, allowing melt resistivity values more than a factor of two different from that calculated from the mean. The conductor depth beneath the Hararo profile is similar; lacking samples from there, we assumed the same melt resistivity value when interpreting that profile.

In the model of the Dabbahu profile (Figure 6), resistivity contours for the two main conductors were roughly circular, and hence so were inferred melt fraction contours, ignoring depth (i.e. pressure and temperature) changes in melt resistivity. For the Moho-straddling conductor, converting resistivity to melt fraction using the parallel conducting pathways model (to get the minimum amount) indicated it decreased approximately linearly from a maximum of 13% to 3% at 13 km distance. The assumption of 2D modelling is that structure continues unchanged in the along-strike direction, but we adopted spherical symmetry to terminate the body. Integrating the linearly varying melt fraction over a sphere of radius 13 km (neglecting melt at lower fractions), it contains a total melt volume of approximately 500 km^3. The shallower conductor beneath the rift axis contains approximately 25 km^3 melt, accounting for the higher melt resistivity owing to its shallower depth and lower temperature. Beneath the Hararo profile, the minimum resistivity value in the model of Figure 6 implies 5.3% melt. In this case, the approximately circular contours of the main conductor are well fit by an exponential decay in melt fraction with distance, given by $f = 0.0527 \exp(-0.105r)$, where f is melt fraction and r is distance (in km) from the centre. Integrating out to 5 km distance, where there is about 3% partial melt (again, neglecting melt at lower fractions), gives a total melt volume of 20 km^3. Melt beneath the Hararo segment is present throughout the lower crust, making the spherical symmetry assumption less reliable. In fact, this estimate neglects melt to the west of the rift axis, including areas where the amount of melt rises to above 3% again. However, the neglected melt will not bring the total to more than a fraction of that inferred beneath the Dabbahu segment.

Although Paper 1 provided compelling evidence for large quantities of magma in the lower crust and mantle where the Badi volcano projects onto the Dabbahu profile, regularised modelling does not constrain how this magma is distributed. Geochemical arguments favour mantle magma concentrated into sills, rather than one large chamber (e.g. Maclennan et al., 2001). Such a model would not be produced by our inversion scheme, since regularisation would discriminate against the associated rapid vertical variations in resistivity. However, by dividing the Moho-straddling conductor in the best-fitting regularised model into a series of resistive bands separated by conducting layers (representing the sills) and re-running the inversion, we have produced a sill-like model (Figure 9). The horizontal discretisation of our model space represents the resolution of the data, so there are relatively few bands and the deeper ones are thicker. The resistive bands are compensated for by even lower resistivity in the conducting layers to maintain the overall conductance. The vertical breaks in the resistive material between the sills are not necessary to fit the data, but are introduced to provide a pathway for the melt to flow upwards, as in geochemical models. It would be possible to have a more realistic model with more, thinner bands; the model of Figure 9 was produced to illustrate that sill-like models are also a feasible explanation of our data. In general, the resistivity of the resistive background is

controlled by the TM mode data, whilst that of the conductive sills by the TE mode data (Berdichevsky, 1999). In this case, we imposed a modest resistivity (100 Ωm) on the layers between the sills, and allowed the resistivity of the remaining blocks to vary, providing an equally good fit to the TE mode data (Figure 10). The slight degradation in the fit to the long period TM mode data could be overcome by adjusting the resistive structure between the sills. The decrease of the minimum resistivity with depth could reflect the decrease in melt resistivity with depth, a variation we have again neglected when estimating melt fractions from bulk resistivity in this sill-like model. In this case, the minimum resistivity is 1.89 Ωm, a little more than half that of the model of Paper 1, implying >22% partial melt. Again, we calculated volumes assuming spherical symmetry, and calculated volumes in disks with > 3% melt, ignoring regions with lower melt fractions. Similarly, we treated the melt fraction as linearly increasing through the disk to its maximum value in each case. The result is a slightly higher minimum melt volume (~ 600 km^3) than when the conductor is a single body (~500 km^3; Paper 1).

Seismic evidence supports the existence of significant amounts of melt in the crust and mantle in our study region. There are broad, pronounced low velocity features over the area of our profiles from both surface wave up to 12 s period (Guidarelli et al., 2011) and P_n (Stork et al., 2013) studies. High upper crustal seismic anisotropy values are attributed to melt pockets in cracks oriented parallel to the rift segment axes (Keir et al., 2011). Through a combination of numerical modelling and geochemistry, Armitage et al. (2015) provide strong evidence that lithospheric melt is necessary to explain features of the seismic data. Crustal receiver functions typically have high V_p/V_s values (Hammond et al., 2011). Receiver function studies suggest a difference in crustal structure either side of the current rift axis (Hammond et al., 2011), associated with the migration of the Afar triple junction and the Red Sea rift axis over time. To its west, the crust is thinner and contains more partial melt (higher V_p/V_s); to its east, it is thicker and retains a more continental-like signature, even though it is still stretched and intruded. Our Dabbahu segment model, whose profile lies on a short segment of Hammond et al.'s (2011) > 300 km-long profile C-C', also has a difference in structure either side of the rift axis, with no indication of significant amounts of melt to its east, consistent with the seismic interpretation. Our Hararo profile is between their profiles B-B' and C-C'. Their more southerly B-B' profile has partial melt distributed across both sides of the rift axis ($V_p/V_s > 2.0$), again consistent with our MT model (in fact, our more conductive region is to the east of the axis). B-B' is to the south of the magmatic segment, so the comparison may not be entirely appropriate, but we note that multiples from which the receiver functions are calculated are sensitive to a region of approximately 25 km diameter from the seismic station, which is less than the distance of our Hararo profile from B-B'. In striking agreement with our results, Belachew (2012) finds, from P- and S-wave tomographic inversion of ~37000 local earthquake phases from ~1300 earthquakes (with hypocentre relocation), two pronounced low velocity zones, beneath Dabbahu volcano and to the west of the AVC, extending to depths of 28 km (the maximum in the tomography model). The zone to the west of the AVC is at the same distance from the rift axis as our mantle-straddling conductor on the Dabbahu and Teru profiles from depths of 18 km, but closer to the axis at shallower depths, even extending both sides of it below 8 km depth. Resolution is not sufficiently good to distinguish unambiguously the continuity or otherwise between the low velocity zones, but there is a suggestion that the zones beneath Dabbahu and to the west of the AVC are

connected along-axis beneath 13 km. Note that the Dabbahu low velocity zone extends into the mantle (in fact, to 28 km, the maximum depth of the tomography model), in better agreement with the regularised model shown in Figure 6 than that in which we impose a resistive mantle. Converting a 0.2 km/s V_p reduction to a minimum of 1-4% melt (Schmeling, 1985; Magde, 2000), Belachew (2012) infers at least 7-12% partial melt to explain these velocity anomalies. He also finds low V_p velocities in the lower crust in the area of our Hararo profile; they are particularly pronounced around 18 km depth and much closer to normal by 23 km depth. However, there is no evidence from the tomography results of the low velocities being concentrated to the east of the rift axis there.

Our Hararo profile is just to the north of the site of the Tendaho geothermal prospect, which has and continues to be investigated by a number of geophysical and other methods. Here, structure of the top 5 km is of particular interest, and a series of MT studies have collected data to periods of up to 1000 s, showing crustal resistivities at least as low as in our Hararo profile model (Didana et al., 2014). The almost ubiquitous near surface conductor in our models is also present. A sub-vertical conductive feature (Kalberkamp, 2009; Didana et al., 2014) potentially mapped a feed for the shallow heat reservoir, which achieved temperatures of 300°C at 300 m depth (Aquater, 1996). Magnetic and gravity data have been collected to seek confirmation that this is a fracture zone that could form a potential pathway for hydrothermal fluids feeding the shallow reservoir (Lemma and Hailu, 2006).

The most striking feature of the Teru profile model (left-most model in Figure 6) is the extremely conductive zone at its northern end. From petrological, seismic and remote sensing information, Field et al. (2012) inferred a substantial and long-lived magma storage region between approximately 1.5 and 5.5 km depth beneath the active Dabbahu volcano, with sills the most favoured geometry. The maximum conductivity in our model is at ~6.5 km depth, and we are unable to fit the data with a conductor confined to the top 5 km or so. The largest percentage P-wave velocity reduction beneath Dabbahu in the tomography model of Belachew (2012) occurs at 8 km. However, although the first-order agreement is good, there are several challenges to a more detailed interpretation. The average resistivity in the crust near Dabbahu volcano is of order 0.5 Ωm. This is typical of or lower than values for pure basaltic melt of most compositions at crustal depths and temperatures (Pommier and Le Trong, 2011). The wide range of erupted products from the Dabbahu volcano implies considerable variation in melt composition and conditions. For instance, parent basaltic melt water content is 0.4-0.5 weight %; however, the recently erupted, much more evolved, lavas have water content up to 5.8 wt % (Field et al., 2012). The very evolved rhyolites (pantellerite and commendite) comprise less than 5% of the erupted products, but require ~80% crystallisation in the top 6 km of the crust (Field et al., 2013). More generally, we might expect to encounter changing melt composition, and hence resistivity, associated with changing melt fractions as magma cools and crystallises. Melt resistivity is strongly dependent on SiO_2 and water content over the range of permissible values, which could encompass values of 47-70 % and 0.4-8 % respectively (Field et al., 2012, 2013); this will change melt resistivity by more than an order of magnitude (Pommier and Le Trong, 2011; Laumonier et al., 2015). Even the possible 1% change in Na_2O and range of pressures and temperatures encountered will have a noticeable impact. Modelling the possible melt supply and evolution, and associated variations in its resistivity, is beyond the scope of the present study, and in

any case is subject to a great degree of uncertainty. Whatever compositions and hence melt resistivities are assumed, and regardless of the ambiguities associated with the MT model, it indicates that there is a resolvable magma reservoir of (close to) pure melt associated with the volcano. A typical evolved composition from melt inclusions hosted in feldspars (Field et al., 2012) has $SiO_2 = 72.1 \pm 1.4$, $Na_2O = 5.9 \pm 0.41$ (both weight %, and 1 standard deviation uncertainties), P = 250 MPa, T = 1200°C; Pommier and Le Trong (2011) predict a melt resistivity of 0.16 Ωm if we assume their highest (5.8%) H_2O content, lower than for basaltic melt but markedly higher than the lowest resistivity seen in the conductor. Laumonier et al.'s (2015) investigation of the conductivity of a silica-rich melt has found values of typically half an order-of-magnitude higher than those of Pommier and Le Trong (2011), dependent on temperature and water content (their Fig. 9). Hence we have assumed a melt resistivity of 0.1 Ωm, giving the melt percentages shown in Figure 11. The melt region extends to below the 15 km depth plotted, but is ignored in our estimates of the melt volume since resolution there is poorer. We also assume the magma body is symmetric about site 104, using the better constrained structure to the south to define a set of nested cylinders with decreasing amounts of melt with lateral distance from site 104. These assumptions, and the limitations from having interpreted a particular 2D model, mean that the melt volume inferred is highly uncertain. Note that these estimates are also conservative since they are based on the parallel conducting pathway model, which is appropriate when melt is arranged in oriented melt pockets, i.e. the sub-surface is anisotropic, but there are virtually no differences between the phases of the two modes in the northern Teru line data that are normally taken as an indication of electrical anisotropy. If we treat the amount of melt in each cylinder or annulus as constant at the mid-value of the range, we get a total indicative melt volume of 80 km^3, about three times that in the conductor directly beneath the Dabbahu segment rift axis, less than the total eruptive volume from Dabbahu (> 115 km^3; Field et al., 2013), and substantially less than beneath the deeper conductor close to the Badi volcano (500 km^3; Paper 1).

Ferguson et al. (2013) analysed both on- and off-axis lavas from the Dabbahu segment near our profile (from the AVC and Badi, respectively; see locations on Fig. 2), and found them to have different chemical signatures. The on-axis lavas were extracted rapidly and/or without chemical interaction, whereas the off-axis lavas re-equilibrated in the upper mantle. Our off-axis mantle magma reservoir is consistent with Ferguson et al's (2013) re-equilibration zone, and the lack of a deeper conductor beneath the axial rifting region supports rapid extraction there. In the lower crust beneath the Dabbahu profile, there is a conducting pathway between the off- and on-axis conductors (e.g. Paper 1, Fig. 3), albeit with a slight resistivity increase. However, breaking the conducting pathway between them (in both the regularised and sill-like model) does not noticeably alter the fit to the data, so we cannot distinguish between separate and connected magma sources. The possibility of a rift jump to accommodate the eastward migration of the Red Sea rift axis over time is suggested by the two partial melt locations beneath the Dabbahu profile. Consistent with the conclusions of Ferguson et al., (2013), Medynski et al. (2015) find that the off-axis reservoir has not supplied the recent dykes, but that it was the main focus of magma accumulation prior to 15 ka, and has been regularly supplied since. They suggest that the current rift axis has been active for the last 30 kyr, but its magma supply has diminished over the last 20 kyr. Daniels et al. (2014) drew a similar conclusion on the basis of numerical modelling of the heat flow equation: more than one locus of

heating is required, to prevent significant localised ductile stretching that would otherwise by now have weakened and thinned the crust by far more than that observed. As already noted, the asymmetric seismic velocity and resistivity structure either side of the current rift axis is consistent with it having migrated. Although much of the lower crust is conductive between the projection of the Badi and the Dabbahu volcanoes onto our Teru profile, we expect on the basis of the geochemistry that the two are separate. Thus we have imaged four separate magma/partial melt regions – beneath the rift axis, the Badi and Dabbahu volcanoes on the active Dabbahu segment, and concentrated to the east of the rift axis beneath the inactive Hararo segment – with a conservative combined melt volume of > 600 km^3, using the differences in composition, temperature and depth of the sources to provide the most reliable melt resistivities from which these volumes were inferred.

The Afar region is thought to be a region of incipient slow sea-floor spreading, with magmatic processes far more important than tectonic ones. To what extent crust being generated there is ocean-like, whether there is any residual influence from the mantle plume(s) that impinged on the region ~45 Ma, and how and where melting occurs, remain matters of debate (e.g. Armitage et al., 2015). The limited depth extents of our profiles mean we are unable to contribute to the discussion on melting depths and processes, and symmetry or otherwise of melt regions generated by mantle upwelling or buoyancy forces (especially as the crust beneath our profiles is much thicker than beneath mid-ocean ridges), but we can compare our results with shallower images, both electrical and seismic, of mid-ocean ridges (at a variety of spreading rates) to assess the extent to which they have features in common, bearing in mind that mid-ocean ridge environments are profoundly affected by hydrothermal circulation.

Beneath two profiles crossing the fast-spreading East Pacific Rise (EPR), sub-vertical conductors in the mantle have been interpreted to contain high melt concentrations (Baba et al., 2006; Key et al., 2013). Baba et al. (2006) prefer an anisotropic model with a flat resistive-conductive interface at about 60 km depth with a highly conductive across-ridge conductor below, and a vertical current sheet in the ρ_{zz} component beneath the ridge axis. Key et al. (2013) infer virtually no anisotropy except for slight enhanced conductivity in the ρ_{zz} component to the east of the ridge in the shallow mantle. In the more northerly location, the conductor was offset from the rift axis at depth, it impinged on the base of the crust where there was a low seismic velocity anomaly (Toomey et al., 2007), and it was interpreted as a porous melt channel rapidly delivering magma to the crust (Key et al., 2013). In the part of Afar we investigated, the highest mantle conductivities are also offset from the rift axes, and the base of the crust and uppermost mantle are seismically slow (Guidarelli et al., 2011; Stork et al., 2013); we lack the depth penetration to determine whether these broad conductors become more laterally confined at depth. Magma is stored in the crust in both axial and off-axis (4-8 km from the axis) locations beneath the EPR, in the latter, in partially molten lower-crustal sills (Canales et al.; 2012); although there was mixing between the two, lavas erupted off-axis had more variable composition (Perfit et al., 1994). Beneath the Dabbahu segment, there is considerable along-axis compositional variability (comparing lavas from the AVC and Dabbahu volcano), and there is geochemical evidence against mixing between the axial and off-axis magmas (which are further apart than at the EPR). Provisional 3D modelling (Hautot et al., 2012) indicates axis-parallel continuity of the lower-crustal conductors in Afar, but there are no associated surface eruptions. Similarly, at the intermediate spreading rate

Juan de Fuca ridge, an off-axis lower crustal melt lens (interpreted as a sill) a few kilometres long in the ridge-parallel direction and a shallower axial magma chamber were imaged by seismic reflection (Canales et al., 2009).

Studies of the slow-spreading mid-Atlantic ridge (MAR) have imaged transiently- or fluctuatingly-supplied crustal magma chambers, with variability on timescales up to ~ 2 Myr and over distances less than 80 km (e.g. Karson et al., 1987), but again provided no evidence of substantial amounts of melt in the upper mantle. A multi-technique study of the magmatically active Reykjanes Ridge indicated a transient magma chamber in the crust, similar to those observed at faster spreading ridges (e.g. Sinha et al., 1997). A seismic reflection survey of the Lucky Strike section of the MAR indicated an axial magma chamber, with median valley faults continuing down to or beneath the chamber (Singh et al., 2006). The width of the faulted region is similar to that for Afar magmatic segments, but does not have the fault density asymmetry about the rift axis observed over the Dabbahu segment (Rowland et al., 2007) that our shallow sub-vertical conductor to the west of the rift axis (between sites 807 and 811 in Fig. 9) is consistent with, nor does it have such a high fault density. Also, Wright et al. (2006) estimate that normal faults only extend to a depth of 2 km beneath the Dabbahu segment. Like Afar, both of these MAR areas are possibly influenced by mantle plumes. In an unaffected area further south, Canales et al. (2000) deduced up to 17% partial melt (if melt inclusions have large aspect ratios) in the middle and lower crust beneath the ridge.

Comparing the volumes of magma available in our models to those intruding during a dyking cycle (which happens every ~500 years) or required to build the full thickness of the crust (rather than just intruding part of it as it is stretched and thinned) at the far-field spreading rate indicates they contain sufficient for at least several tens of kyr beneath the Dabbahu segment (the timescale over which MAR segments can change from being magma-starved to magma-enriched; Canales et al., 2000). However, there is doubt from the geochemical analyses as to whether the mid-segment axial magma chamber is connected to the deeper off-axis one and/or to the one beneath the Dabbahu volcano at the northern end of the segment, so we cannot rule out a transient supply to the axial chamber. The inactivity on the Hararo segment, where there are also notable volumes of magma in the deep crust, again displaced from the rift axis, suggests this might be the case. However, InSAR data indicate that the Dabbahu segment axial magma chamber barely inflated or deflated during the recent dyke intrusions it sourced (Hamling et al., 2009). Thus the geometry and temporal variability of the plumbing systems responsible for extrusive and intrusive volcanism in the region remain uncertain.

5. Conclusions

We have presented MT data and 2D models from three profiles in the Afar region of Ethiopia, two over and near the active Dabbahu magmatic segment, the other over the currently inactive Hararo segment. The low resistivities encountered in the cross-segment profiles suggest that there are significant amounts of magma and partial melt beneath both segments, much more than is required to supply the recent dyke intrusions and eruptions, and sufficient to build the crust at the far-field spreading rate for of order a few tens of kyr. Inferred melt volumes are higher beneath the active

segment, and a substantial amount is in the mantle to the west of the rift axis. However, there are still significant quantities of melt beneath the Hararo segment, but in this case, more widely dispersed laterally and, depth-wise, mainly straddling the Moho. Beneath the Dabbahu volcano, our model has resistivities so low as to indicate pure melt in the shallow crust and implies a large melt volume. These inferences of large quantities of melt and its location are broadly in agreement with conclusions from seismological information, although the distribution and melt fractions are not identical. Petrological analysis of samples from the Badi volcano to the west of the Dabbahu rift axis and recent rift axis eruptions give melting depths of 75-100 km. Badi samples are from magma that has re-equilibrated near the top of the mantle, in agreement with the low resistivity body in our model, in contrast to those from axial eruptions, which are transported quickly from their melting depth. This mantle melt could as easily be contained in sills as in a single magma body. A summary cartoon of the melt distribution is given in Figure 12. The lack of inflation and deflation signatures associated with the recent series of dyke intrusions beneath the Dabbahu segment suggests a continuous magma supply. However, InSAR results indicate that a region to the south of the Dabbahu segment, between that and the Hararo segment, is currently deflating, perhaps implying a lateral movement of magma to supply the current dyking episode (T Wright, pers. comm., 2012). Our results indicate that there is magma available there. Three-dimensional modelling of the data, including a few sites to the north of the Hararo segment line not shown in Figure 2, may indicate whether there could be a connection between the zones of partial melt beneath the Dabbahu and Hararo segments.

Acknowledgements

This research has been supported financially by NERC (grant NE/E007147/1 and PhD studentship for NEJ), the School of GeoSciences (MSc by Research MTEM Partial Scholarship to MD), CNRS (funding for SH), and in-kind by equipment loans from the NERC Geophysical Equipment Facility (GEFSC loans 855, 866 and 907), and the Geophysical Instrument Pool Potsdam (part of GeoForschungsZentrum) through the auspices of Oliver Ritter and Ulrich Kalberkamp (formerly of BGR, Hannover). The Geophysical Observatory (part of the Institute for Geophysics, Space Science and Astronomy), Addis Ababa University and the Geological Survey of Ethiopia are thanked for extensive logistical support, as is Yohannes Lemma (Geological Survey of Ethiopia) for help with the fieldwork. The Afar Regional Government enabled access to the field area and provided significant practical assistance. Helicopter access to the Dabbahu rift was ably and cheerfully provided by pilot Chris Stewart from Everett Aviation (Kenya). SPOT imagery was provided to SH by CNES, France. We also acknowledge discussions with and results in advance of publication from Afar Rift Consortium colleagues and Project Partners, in the UK, Ethiopia, USA and New Zealand. We thank the reviewers (Ian Ferguson and one anonymous) and the editor David Ferguson for their constructive comments.

References

Abbate, E, Passerini, P and Zan, L, 1995 Strike-slip faults in a rift area: A transect in the Afar triangle, East Africa, *Tectonophys.*, **241**, 67-97

Aizawa, K, et al, 2011. Temporal changes in electrical resistivity at Sakurajima volcano from continuous magnetotelluric observations, *J. Volc.. Geotherm. Res.*, **199**, 165–175

Aquater, 1996, Tendaho geothermal project, final report, Ministry of Mines of Ethiopia and Ministry of Foreign Affairs of Italy, San Lorenzo in Campo, Italy (unpublished)

Armitage, J J, Ferguson, D J, Goes, S, Hammond, J O, Calais, E, Rychert, C A and Harmon, N, 2015. Upper mantle temperature and the onset of extension and break-up in Afar, Africa, *Earth Planet. Sci. Letts.*, **418**, 78-90

Atnafu, B, et al., 2015. Reading history from Afar, *Eos,* **96,** doi:10.1029/2015EO022789

Ayele, A, *et al.*, 2009, September 2005 mega-dike emplacement in the Manda-Harraro nascent oceanic rift (Afar depression), *Geophys. Res. Lett.*, **36**, L20306, doi:10.1029/2009GL039605, 2009

Baba, K, Chave, A D, Evans, R L, Hirth, G and Mackie, R L, 2006. Mantle dynamics beneath the East Pacific Rise at 17°S: Insights from the Mantle Electromagnetic and Tomography (MELT) experiment, *J. Geophys. Res.*, **111**, B02101

Battistelli, A, *et al.*, 2002. Reservoir engineering assessment of Dubti geothermal field, Northern Tendaho Rift, Ethiopia, *Geothermics*, **31**, 381-406, doi:10.1016/S0375-6505(01)00039-6

Belachew, M, *et al.,* 2011, Comparison of dike intrusions in an incipient seafloor-spreading segment in Afar, Ethiopia: Seismicity perspectives, *J. Geophys. Res.*, **116**, B06405, doi:10.1029/2010JB007908

Belachew, M, 2012, Dynamics of dike intrusions and 3D velocity structure beneath an incipient seafloor spreading center in Afar, Ethiopia, unpublished PhD thesis, University of Rochester, USA

Berdichevsky, M N, 1999, Marginal notes on magnetotellurics, *Surv. Geophys.*, **20**, 341-375

Bologna, MS, Padilha, AL, Vitorelli, I and Padua, MB, 2011, Signatures of continental collisions and magmatic activity in central Brazil as indicated by a magnetotelluric profile across distinct tectonic provinces, *Precambr. Res.*, **185**, 55-64

Brasse, H and Eydam, D, 2008, Electrical conductivity beneath the Bolivian Orocline and its relation to subduction processes at the South American continental margin, *J. Geophys. Res.*, **113**, B07109, doi: 10.1029/2007JB005142

Bridges, D, Mickus, K, Gao, S, Abdelsalam, M and Alemu, A, 2012, Magnetic stripes of a transitional continental rift in Afar, *Geology*, **40**, 1-4

797 Caldwell T G, Bibby H M and Brown C, 2004, The magnetotelluric phase tensor,
798 *Geophys. J. Int.*, **158**, 457-469
799
800 Canales, J P, Collins, J A, Escartín, J and Detrick, R S, 2000, Seismic structure across
801 the rift valley of the Mid-Atlantic Ridge at 23°20' (MARK area): Implications for
802 crustal accretion processes at slow-spreading ridges, *J. Geophys. Res*., **105**, 28411-
803 28425
804
805 Canales, J P, *et al.*, 2009, Seismic reflection images of a near-axis melt sill
806 within the lower crust at the Juan de Fuca ridge, *Nature*, **460**, 89-94,
807 doi:10.1038/nature08095
808
809 Canales, J P, *et al.*, 2012. Network of off-axis melt bodies at the East Pacific Rise,
810 *Nature Geosci.*, **5**, 279-283, doi: 10.1038/ngeo1377

811 Chave, A and Jones, A G (editors), 2012, *The Magnetotelluric Method: Theory and*
812 *Practice*, Cambridge University Press, Cambridge, UK

813 Chave, A D and Thomson, D J, 1989, Some comments on magnetotelluric response
814 function estimation. *J. Geophys. Res*., **94**, 14215- 14225
815
816 Chernet, T, 2012, Dallol Volcano and Danakil Depression, Ethiopia, Magmatic
817 Rifting and Active Volcanism conference, Addis Ababa,
818 http://www.see.leeds.ac.uk/afar/new-afar/conference/talks/Tadiwos.pdf
819
820 Counil, J-L, Le Mouël, J-L & Menvielle, M., 1986. Associate and conjugate direction
821 concepts in magnetotellurics, *Ann. Geophys*., **4**, 115-130
822
823 Daniels, K A, Bastow, I D, Keir, D, Sparks, R S J and Menand, T, 2014. Thermal
824 models of dyke intrusion during development of continent–ocean transition, *Earth*
825 *Planet. Sci. Lett.*, **385**, 145-153, doi: 10.1016/j.epsl.2013.09.018
826
827 Desissa, M, *et al.*, 2013, A mantle magma reservoir beneath an incipient mid-ocean
828 ridge in Afar Ethiopia, *Nature Geosci.*, **6**, 861-865, doi: 10.1038/ngeo1925
829
830 Didana, Y L, Thiel, S and Heinson, G, 2014, Magnetotelluric imaging of upper crustal
831 partial melt at Tendaho graben in Afar, Ethiopia, *Geophys. Res. Lett.*, **41**, 3089-3095,
832 doi: 10.1002/2014GL060000
833
834 Ebinger, C J, *et al*., 2008, Capturing magma intrusion and faulting processes during
835 continental rupture: seismicity of the Dabbahu (Afar) rift, *Geophys. J. Int.*, **174**, 1138–
836 1152
837
838 Ebinger, C, *et al.*, 2010, Length and Timescales of Rift Faulting and Magma
839 Intrusion: The Afar Rifting Cycle from 2005 to Present, *Ann. Rev. Earth Planet. Sci.*,
840 **38**, 437–64
841
842 Ferguson, D, *et al.*, 2010, Recent rift-related volcanism in Afar, Ethiopia, *Earth*
843 *Planet. Sci. Lett.*, **292**, 409-418
844

Ferguson, D J, *et al.*, 2013, Melting during late-stage rifting in Afar is hot and deep, *Nature*, **499**, 70-73

Ferguson, I J, 2012. Instrumentation and Field Procedure, Chapter 9 in *The Magnetotelluric Method: Theory and Practice*, ed. Chave, A D and Jones, A G, p421-479, Cambridge University Press, Cambridge, UK

Field, L P, Blundy, J, Brooker, R A, Wright, T J and Yirgu, G, 2012, Magma storage conditions beneath Dabbahu Volcano (Ethiopia) constrained by petrology, seismicity and satellite geodesy**,** *Bull. Volcanol.***, 74**, 981–1004

Field, L P, Blundy, J, Calvert A and Yirgu, G, 2013, Magmatic history of Dabbahu, a composite volcano in the Afar Rift, Ethiopia, *GSA Bull.,* **125**, 128-147, doi: 10.1130/B30560.1

Grandin, R, *et al.*, 2010, Transient rift opening in response to multiple dike injections in the Manda Hararo rift (Afar, Ethiopia) imaged by time-dependent elastic inversion of interferometric synthetic aperture radar data, *J. Geophys. Res.*, **115**, B09403, doi:10.1029/2009JB006883

Groom, R W & Bailey, R C, 1989. Decomposition of magnetotelluric impedance tensors in the presence of local 3-dimensional galvanic distortion, *J. Geophys. Res.,* **94**, 1913-1925

Guidarelli, M., *et al.*, 2011. Surface wave tomography across Afar, Ethiopia: Crustal structure at a rift triple-junction zone, *Geophys. Res. Lett.*, **38**, L24313, doi:10.1029/2011GL046840

Hamling, I J, Ayele, A, Bennati, L, Calais, E and Ebinger, C J, 2009, Geodetic observations of the ongoing Dabbahu rifting episode: new dyke intrusions in 2006 and 2007, *Geophys. J. Int.,* **178**, 989-1003

Hammond, J O S, *et al.*, 2011, The nature of the crust beneath the Afar triple junction: Evidence from receiver functions, *Geochem. Geophys. Geosys.*, **12**, Q12004, doi: 1029/2011GC003738

Hashin, Z and Shtrikman, S, 1962, A variational approach to the theory of the effective magnetic permeability of multiphase materials. *J. Appl. Phys.*, **33**, 3125-3131

Häuserer M and Junge A, 2011, Electrical mantle anisotropy and crustal conductor: a 3-D conductivity model of the Rwenzori Region in western Uganda, *Geophys. J. Int.*, **185**, 1235–1242

Hautot, S, *et al.*, 2000, The deep structure of the Baringo rift Basin (central Kenya) from 3-D magnetotelluric imaging: Implications for rift evolution, *J. Geophys. Res.,* **105**, 23,493-23,518

Hautot, S, *et al*., 2012, Melt distribution between the crust and mantle beneath the Dabbahu-Manda Hararo rift segment, Afar, from 3D magnetotelluric imaging,

Magmatic Rifting and Active Volcanism conference, Addis Ababa, http://www.see.leeds.ac.uk/afar/new-afar/conference/talks/Hautot.pdf

Hayward, N and Ebinger, C, 1996, Variations in along-axis segmentation of the Afar Rift System, *Tectonics,* **15**, 244-257

Heinson, G, Constable, S and White, A, 2000, Episodic melt transport at mid-ocean ridges inferred from magnetotelluric sounding. *Geophys. Res. Lett.*, **27**, 2317-2320

Hovland, M, Rueslaatten, H and Johnsen, H K, 2008, Hydrothermal salt—but how much?: Reply to Christopher Talbot on his comments to our articles, *Marine Petrol. Geol.*, **25**, 203-4

Jones, A G and Ferguson, I J, 2001. The electric Moho. *Nature*, **409**, 331-333

Kalberkamp, U, 2009, Magnetotelluric measurements to explore for deeper structures of the Tendaho geothermal field, Afar, NE Ethiopia, 23rd Kolloquium Elektromagnetische Tiefenforschung, Seddiner See, Germany

Karson, J P, *et al.*, 1987. Along-axis variations in seafloor spreading in the MARK area, *Nature*, **328**, 681-685

Keir, D, *et al.*,2009, Evidence for focused magmatic accretion at segment centers from lateral dike injections captured beneath the Red Sea rift in Afar, *Geology,* **37**, 59–62

Keir, D, Belachew, M, Ebinger, C J, Kendall, J-M, Hammond, J O S, Stuart, G W, Ayele A and Rowland J V, 2011, Mapping the evolving strain field during continental breakup from crustal anisotropy in the Afar depression, *Nat. Commun.*, **2:285**, doi: 10.1038/ncomms1287

Kelbert, A, Egbert, G D and DeGroot-Hedlin, C, 2012, Crust and upper mantle electrical conductivity beneath the Yellowstone Hotspot Track, *Geology*, **40**, 447-450, doi: 10.1130/G32655.1

Key, K, Constable, S, Liu, L and Pommier, A, 2013. Electrical image of passive upwelling beneath the northern East Pacific Rise, *Nature*, **495**, 499-502

Lahitte, P, Gillot, P Y and Courtillot, V, 2003, Silicic central volcanoes as precursors to rift propagation: the Afar case. *Earth Planet. Sci. Lett.*, 207, 103–116

Lemma, Y and Hailu, A, 2006, Gravity and magnetics survey at the Tendaho geothermal field, Geological Survey of Ethiopia, Addis Ababa, Ethiopia, 23pp (unpublished)

Maclennan, J, McKenzie, D, Gronvöld, K and Slater, L, 2001, Crustal accretion under northern Iceland, *Earth Planet. Sci. Lett.*, **191**, 295-310

MacGregor, L M, Constable, S and Sinha, M C, 1998, The RAMESSES experiment – III. Controlled-source electromagnetic sounding of the Reykjanes Ridge at 57°45'N. *Geophys. J. Int.*, **135**, 773-789

Magde, L S, Sparks, D W and Detrick, R S, 1997, The relationship between buoyant mantle flow, melt migration, and gravity bull's eyes at the Mid-Atlantic Ridge between 33°N and 35°N, *Earth Planet. Sci. Lett.*, **148**, 59-67

McNeice, G W and Jones, A G, 2001, Multisite, multifrequency tensor decomposition of magnetotelluric data, *Geophysics*, **66**, 158-173

Medynski, S, *et al.*, 2015, Stability of rift axis magma reservoirs: spatial and temporal evolution of magma supply in the Dabbahu rift segment (Afar, Ethiopia) over the past 30 kyr, *Earth Planet. Sci. Lett.*, **409**, 278-289, doi: 10.1016/j.epsl.2014.11.002

Miensopust, M P, Jones, A G, Hersir, G P and Vilhjalmsson, A M, 2014, The Eyjafjallajokull volcanic system, Iceland: insights from electromagnetic measurements, *Geophys. J. Int.*, 199, 1187-1204, doi: 10.1093/gji/ggu322

Munoz, G, 2014, Exploring for Geothermal Resources with Electromagnetic Methods, *Surv. Geophys.*, **35**, 101-122, doi: 10.1007/s10712-013-9236-0

Parker, R L and Booker, J R, 1996, Optimal one-dimensional inversion and bounding of magnetotelluric apparent resistivity and phase measurements, *Phys. Earth Planet. Ints.*, **98**, 269-282

Pommier, A and Le Trong, E, 2011, SIGMELTS: A web portal for electrical conductivity calculations in geosciences, *Comp. Geosci.*, **37**, 1450-1459

Ritter O, Junge A and Dawes G J K, 1998, New equipment and processing for magnetotelluric remote reference observation. *Geophy. J. Int.*, **132**, 535-548

Roberts, J J and Tyburczy, J A 1999, Partial-melt electrical conductivity: Influence of melt composition, *J. Geophys. Res.*, **104**, 7055-7065

Rowland, J V, *et al.*, 2007, Fault growth at a nascent slow-spreading ridge: 2005 Dabbahu rifting episode, Afar, *Geophys. J. Int.,* **171,** 1226–1246

Schmeling, H, 1985, Numerical models on the influence of partial melt on elastic, anelastic and electric properties of rocks. Part I: Elasticity and anelasticity, *Phys. Earth Planet. Inter.*, **41**, 34–57

Simpson F, 2000, A three-dimensional model of the southern Kenya rift: departure from two dimensionality as a possible consequence of a rotating stress field, *J. Geophys. Res.*, **105**, 19321–19334

Simpson, F and Bahr, K, 2005, *Practical Magnetotellurics*. Cambridge University Press, Cambridge, UK

Singh, S C, *et al.*, 2006. Discovery of a magma chamber and faults beneath a Mid-Atlantic Ridge hydrothermal field, *Nature*, **442**, 1029-1032

Sinha, M C, *et al.*, 1997. Evidence for accumulated melt beneath the slow-spreading Mid-Atlantic Ridge, *Phil. Trans. R. Soc. Lond. A*, **355**, 233-253

Siripunvaraporn, W and Egbert, G, 2000, An efficient data sub-space inversion method for 2-D magnetotelluric data, *Geophysics*, **65**, 791-803

Sternberg, B, Washburne, J C and Pellerin, L, 1988, Correction for the static shift in magnetotellurics using transient electromagnetic soundings, *Geophysics*, **53**, 1459-1468

Stork, A L, Stuart, G W, Henderson, C M, Keir, D and Hammond, J O S, 2013, Uppermost mantle (P_n) velocity model for the Afar region, Ethiopia: An insight into rifting processes, *Geophys. J. Int.*, **193**, 321-328 (2013)

Talbot, C, 2008, Hydrothermal salt – but how much? *Marine Petrol. Geol.***, 25**, 191-202

Toomey, D R, *et al.*, 2007. Skew of mantle upwelling beneath the East Pacific Rise governs segmentation, *Nature*, **446**, 409-414

Wannamaker, P E *et al.*, 2008, Lithospheric dismemberment and magmatic processes of the Great Basin-Colorado Plateau transition, Utah, implied from magnetotellurics, *Geochem. Geophys. Geosyst.*, **9**, Q05019, doi: 10.1029/2007GC001886

Weaver, J, 1994, *Mathematical methods for geo-electromagnetic induction*. Research Studies Press

Wright, T J, *et al.*, 2006, Magma-maintained rift segmentation at continental rupture in the 2005 Afar dyking episode, *Nature,* **442,** 291–294

Figure Captions

Figure 1. Tectono-magmatic segmentation of the Afar volcanic province, after Hayward and Ebinger (1996). TGD denotes the Tendaho-Goba'ad discontinuity. Earthquake fault plane solutions indicate predominantly normal faulting. Small black dots indicate epicentres of earthquakes recorded October 2005 – April 2006 by a regional temporary seismic array, as described by Ebinger et al. (2008). The box shows the area of Figure 2.

Figure 2. Magnetotelluric site distribution along three profiles, superimposed on the topography: to the north, across (Dabbahu line) and oblique (Teru line) to the active Dabbahu magmatic segment; to the south, across (Hararo line) the inactive Hararo segment. In red, the star marks the site of the 2009 eruption within the Ado'Ale Volcanic Complex (AVC) and the Badi and Dabbahu volcanoes are labelled. The red lines delineate the region of the Dabbahu magmatic segment intruded in the recent dyking episode. The dashed black line indicates the locus of the rift axis through the Hararo magmatic segment.

Figure 3. Scaled TEM decay curves (green symbols) overlain on TE and TM mode apparent resistivity curves (blue and red symbols respectively). Site numbers given in the top left of the plot.

Figure 4. Data pseudo-section for the Hararo profile, with sites arranged from west to east. Upper panels are apparent resistivity, lower panels phase. Left-hand side is TE mode, right-hand side the TM mode. Grey masks areas of missing data.

Figure 5. As for Figure 4 for the Teru profile, with sites plotted south to north.

Figure 6. Resistivity structure beneath the three profiles, embedded in a 3D volume of the region. The Hararo profile is on the right, the Teru profile on the left, and the Dabbahu profile between them. The red crosses are the sites, the red lines show the location of dykes intruded in the current episode, B, D and G are the Badi, Dabbahu and Gab'ho volcanoes respectively, AVC is the Ado'Ale Volcanic Complex, and the black dotted line on the Hararo profile marks the rift axis of that segment. The resistivity scale beneath applies to all three models, with substantial parts of the Teru model saturated at the low resistivity limit.

Figure 7. Data fits for the Hararo profile model, that furthest to the right in Figure 6, from west to east along the profile. Blue (red) symbols and curves are the TE (TM) data and model predictions, respectively. Error bars are one standard deviation. Site numbers are indicated in the top left corner.

Figure 8. Data fits for the Teru profile model, furthest to the left in Figure 6, from south to north along the profile. Legend as for Figure 7.

Figure 9. Sill-like model of the deeper conductor beneath the Dabbahu profile.

Figure 10. Fits to the Dabbahu profile data. Bold colour curves are the predictions of the sill-like model of Figure 9; lighter colour curves are those of the original model

shown in Figure 6. At most sites and periods, the differences are indistinguishable by eye. Legend as for Figure 7.

Figure 11. Blocks of the Teru profile minimum structure resistivity model colour-coded according to their melt amount, for an assumed melt resistivity of 0.1 Ωm and the parallel conducting pathways model. Yellow corresponds to pure melt. The vertical line indicates the assumed axis of symmetry of the conductor when inferring melt volume (see text for details).

Figure 12. Summary cartoon of melt distribution beneath the Dabbahu and Hararo (sometimes referred to collectively as Manda-Hararo) magmatic segments looking approximately north-east, inferred from magnetotelluric data, with support from petrological, seismic, remote sensing and geological information. Blue dashed lines show the locations of the three magnetotelluric profiles.

Table caption

Table 1. Root-mean-square misfits for each site and overall of the 'strike' decomposition model applied simultaneously to the Hararo (top) and Teru (bottom) profiles for their preferred geoelectrical strike directions. Sites are listed from west to east for the Hararo profile, and south to north for the Teru profile.

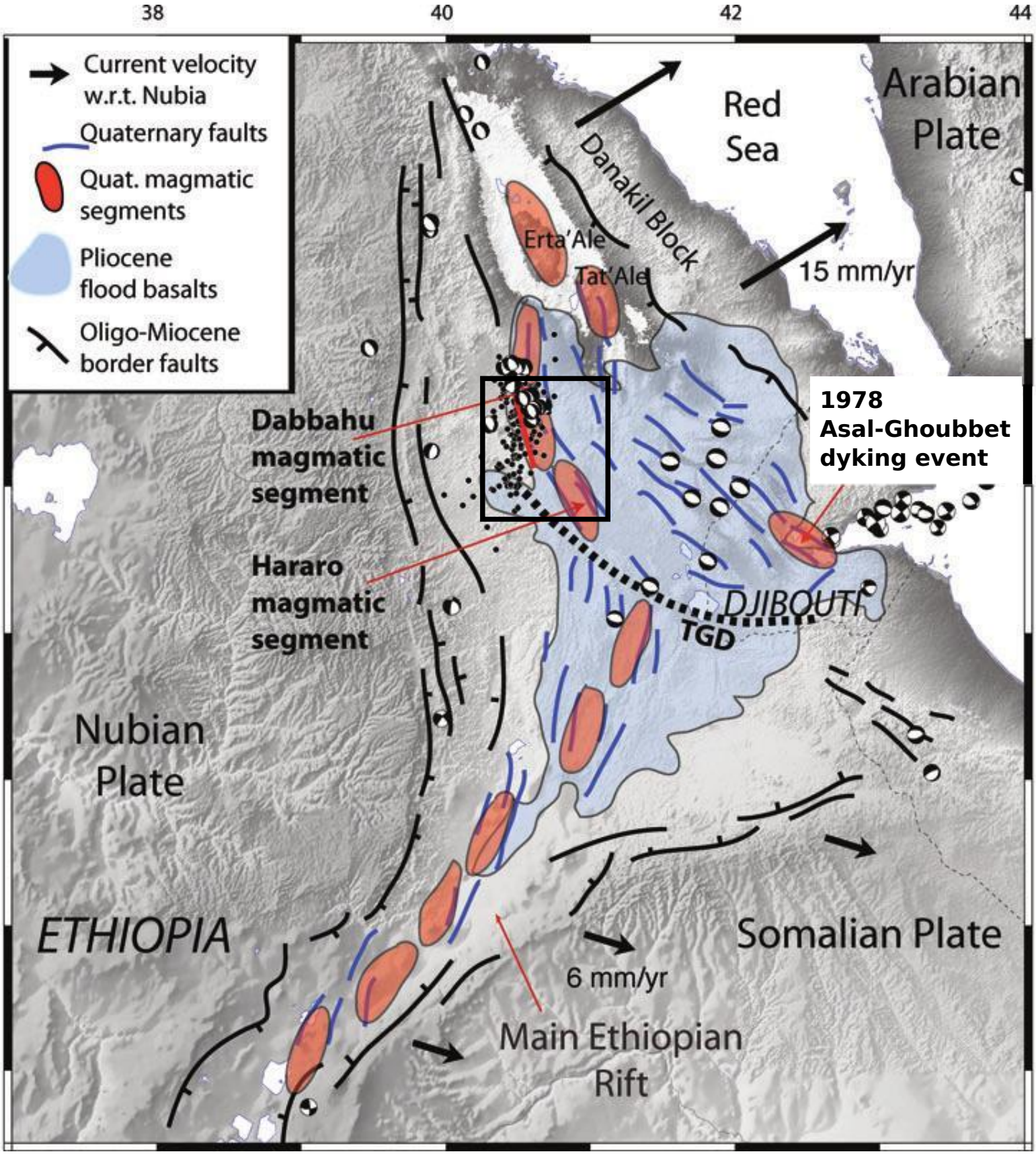
38
40
42
44
14
12
10
8
Current velocity w.r.t. Nubia
Quaternary faults
Quat. magmatic segments
Pliocene flood basalts
Oligo-Miocene border faults
Red Sea
Arabian Plate
Danakil Block
Erta'Ale
Tat'Ale
15 mm/yr
1978 Asal-Ghoubbet dyking event
Dabbahu magmatic segment
Hararo magmatic segment
DJIBOUTI
TGD
Nubian Plate
ETHIOPIA
Somalian Plate
6 mm/yr
Main Ethiopian Rift

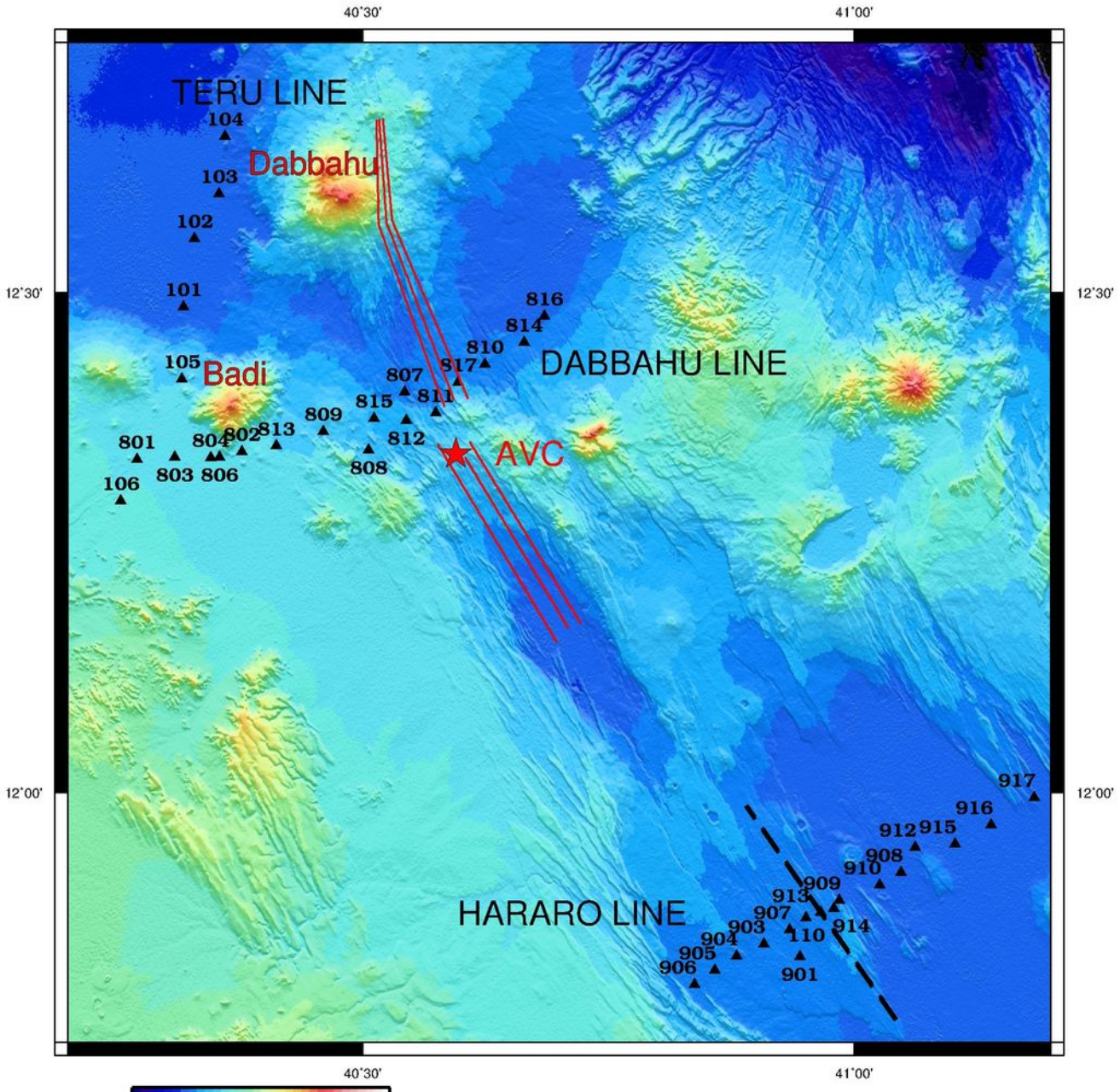
40°30'
41°00'
12°30'
12°00'
TERU LINE
Dabbahu
DABBAHU LINE
Badi
AVC
HARARO LINE
104
103
102
101
105
106
801
803
804
806
802
813
809
815
807
811
817
810
816
814
812
808
917
916
912
915
908
910
909
913
907
903
110
914
904
905
906
901
0
300
600
900
1200
1500
1800
metres

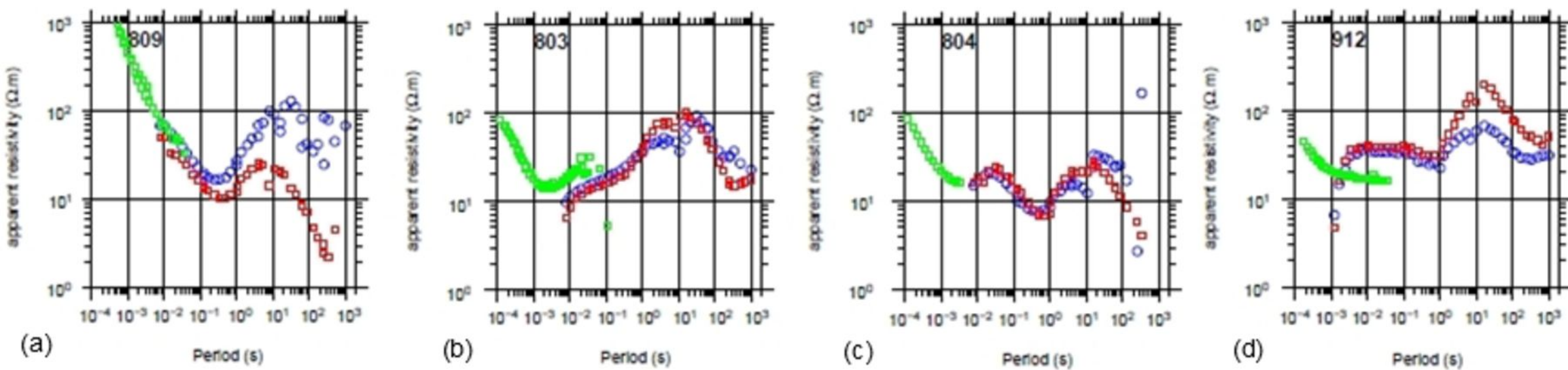
309
803
804
912
apparent resistivity (Ω.m)
Period (s)
(a)
(b)
(c)
(d)

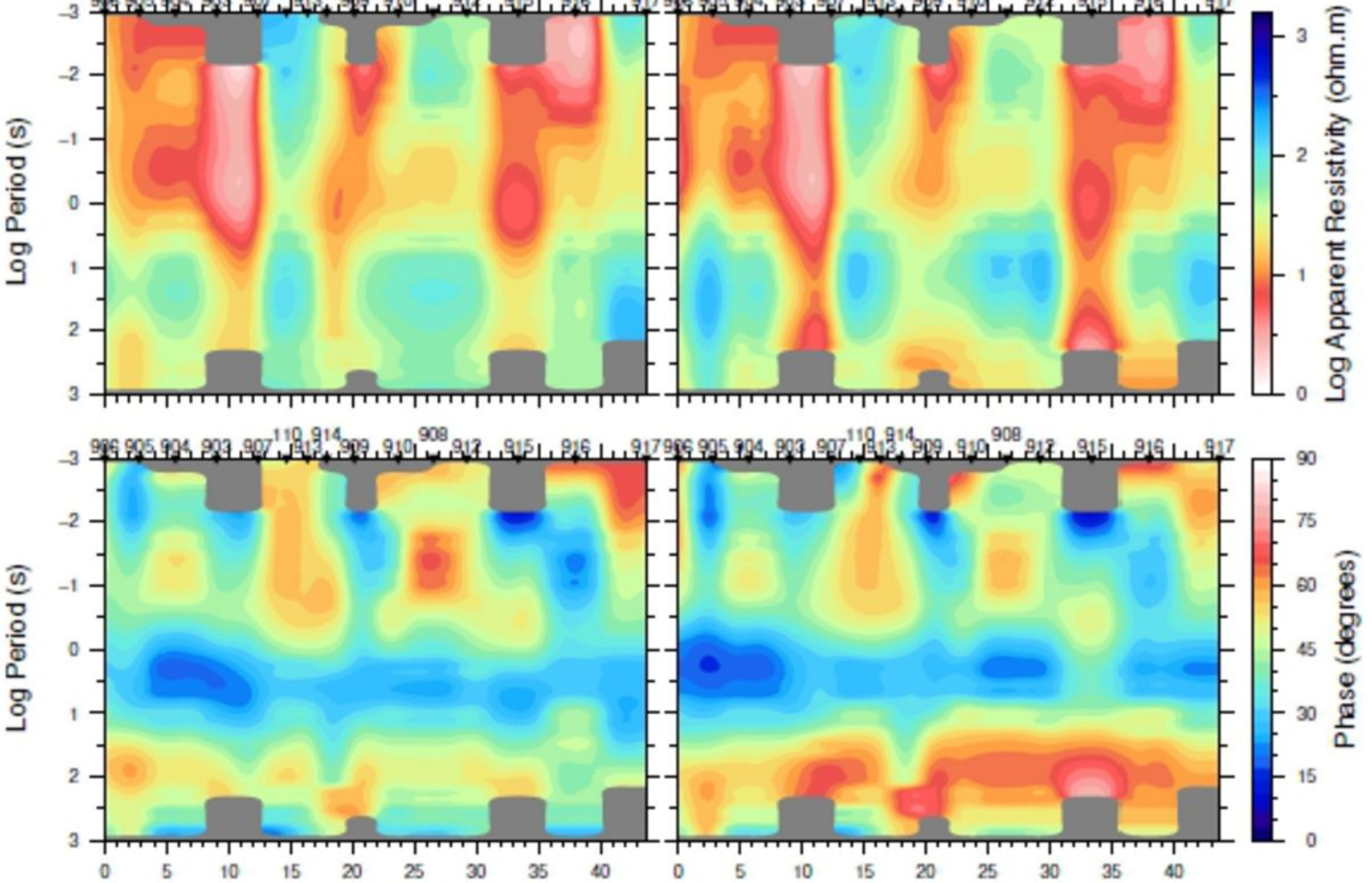
Log Period (s)
Log Apparent Resistivity (ohm.m)
Phase (degrees)

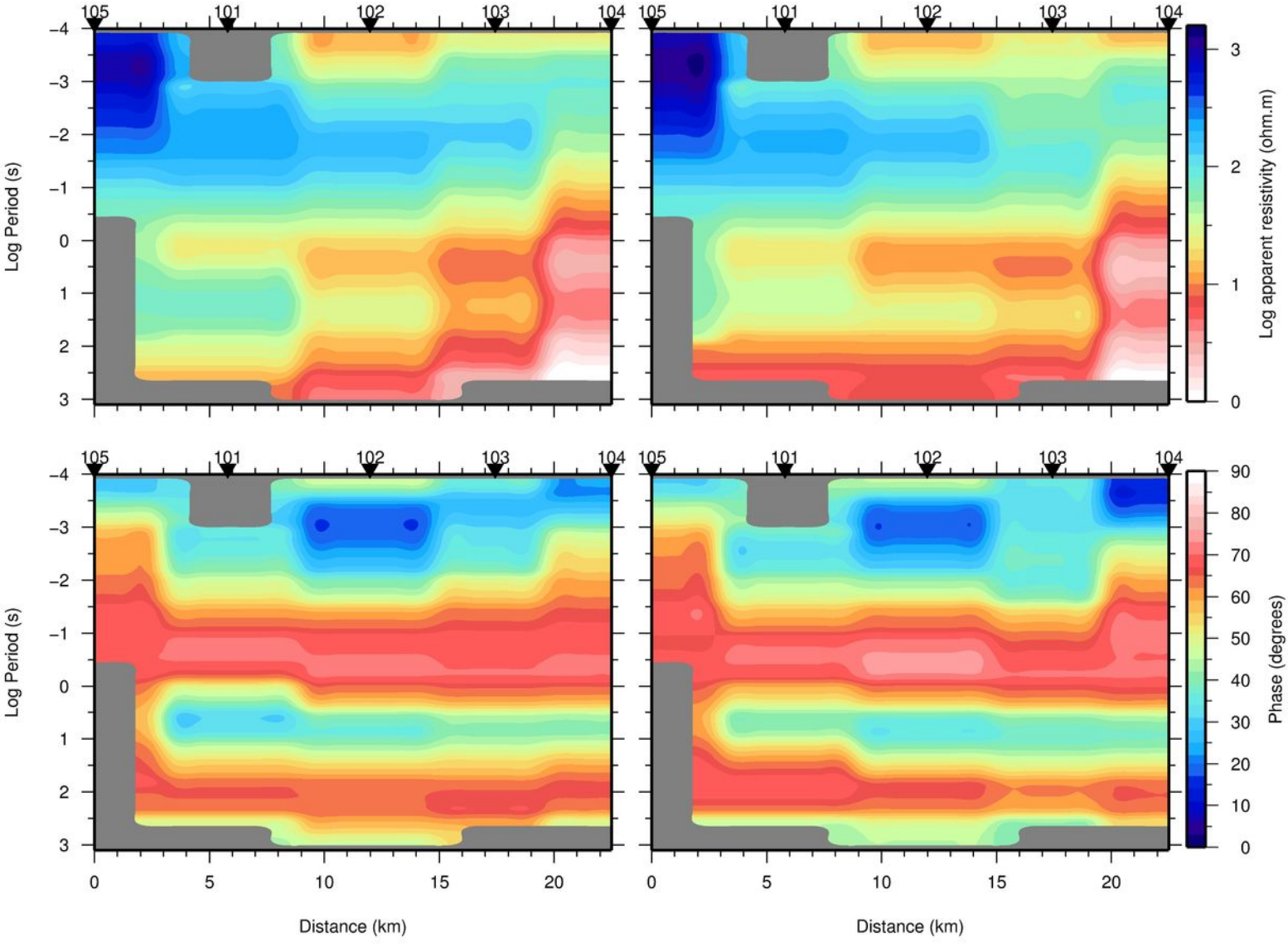
105
101
102
103
104
Log Period (s)
−4
−3
−2
−1
0
1
2
3
Log apparent resistivity (ohm.m)
Phase (degrees)
90
80
70
60
50
40
30
20
10
0
5
10
15
20
Distance (km)

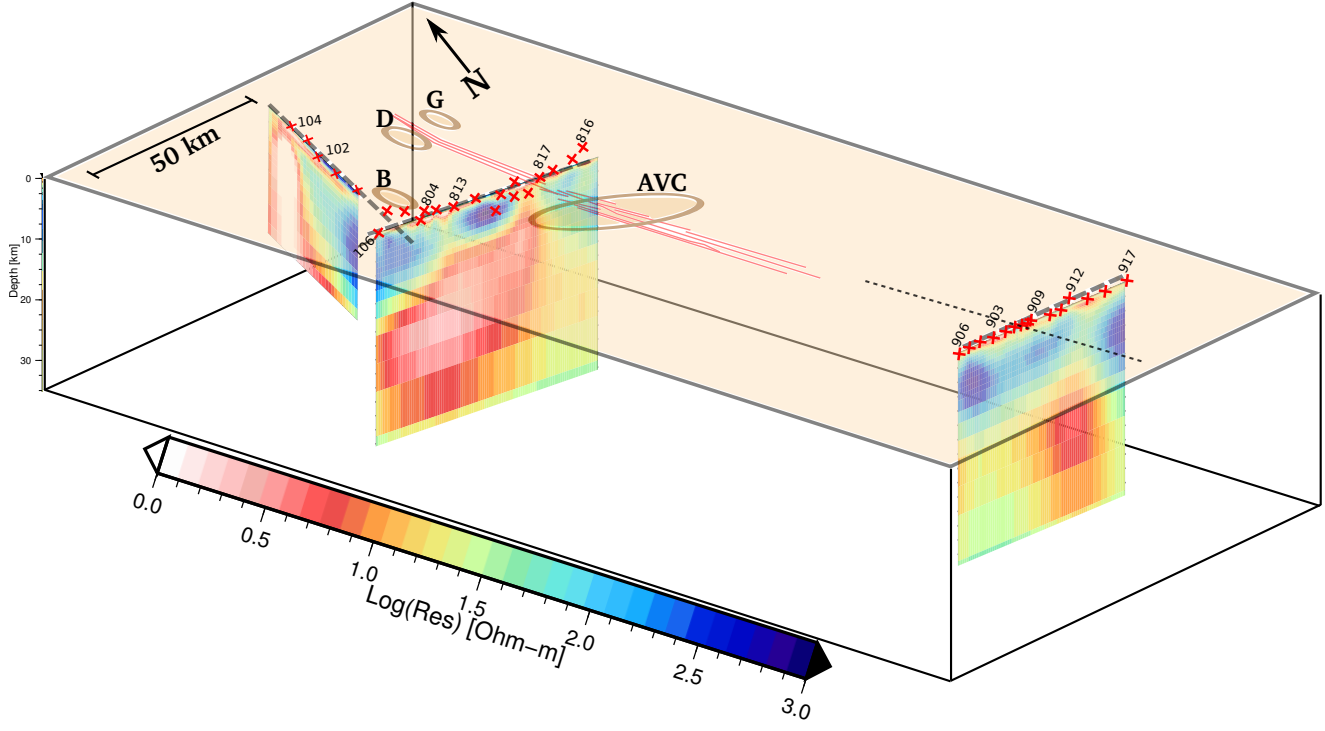
50 km
N
G
D
B
AVC
104
102
106
804
813
816
817
906
903
909
912
917
Depth [km]
0
10
20
30
0.0
0.5
1.0
1.5
2.0
2.5
3.0
Log(Res) [Ohm−m]

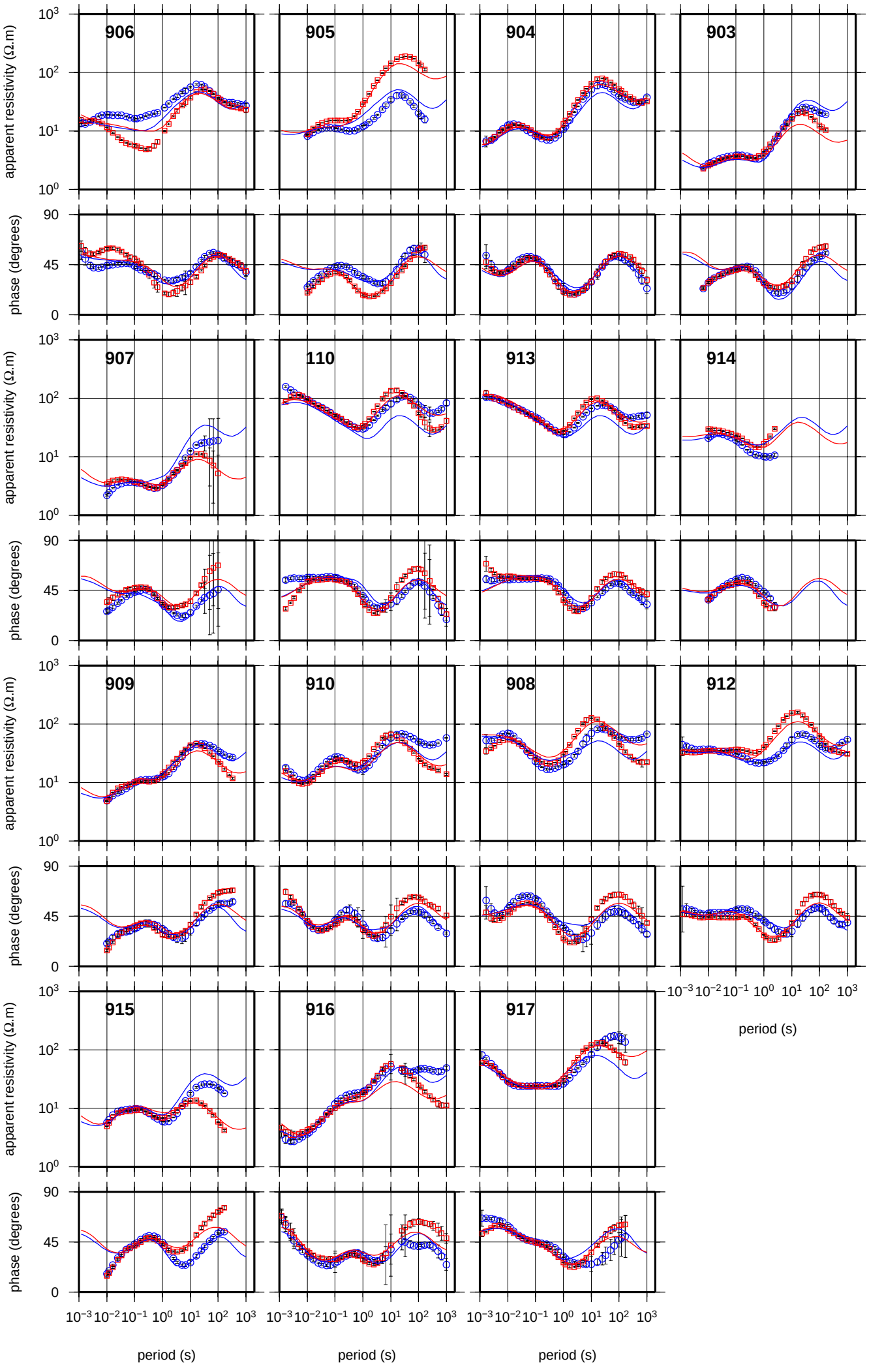
906
905
904
903
907
110
913
914
909
910
908
912
915
916
917
apparent resistivity (Ω.m)
phase (degrees)
period (s)

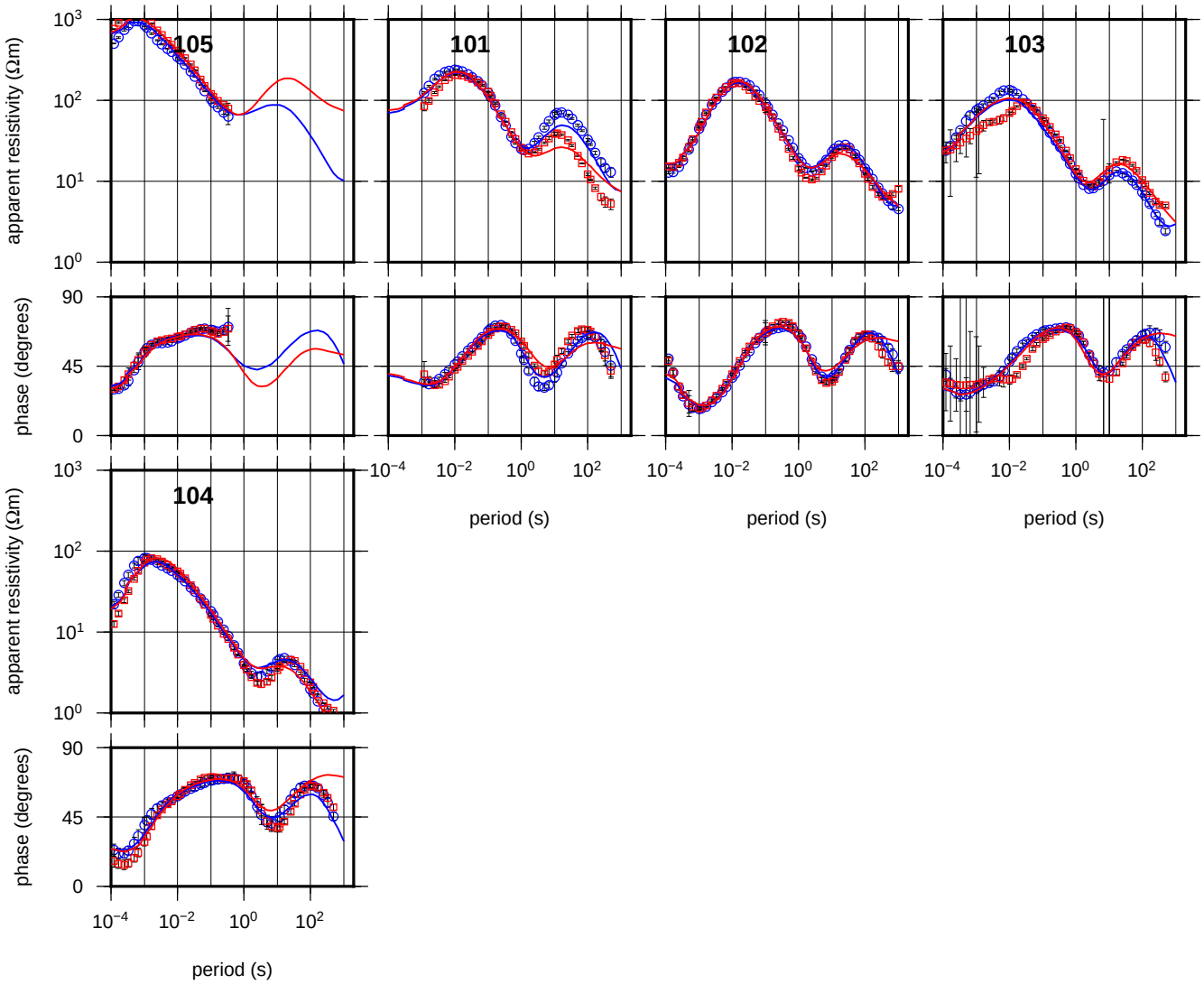
105
101
102
103
104
apparent resistivity (Ωm)
phase (degrees)
period (s)

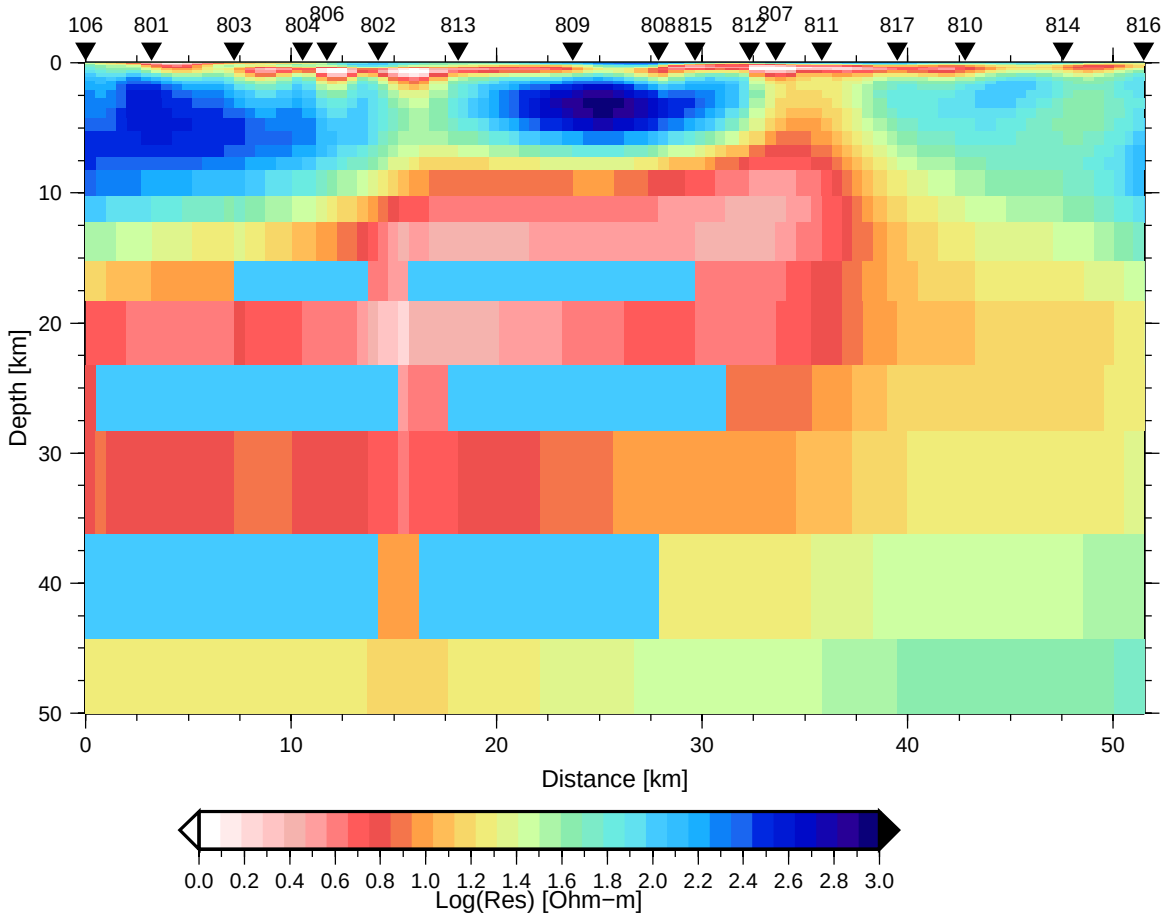
106
801
803
804
806
802
813
809
808
815
812
807
811
817
810
814
816
0
10
20
30
40
50
Depth [km]
0
10
20
30
40
50
Distance [km]
0.0 0.2 0.4 0.6 0.8 1.0 1.2 1.4 1.6 1.8 2.0 2.2 2.4 2.6 2.8 3.0
Log(Res) [Ohm−m]

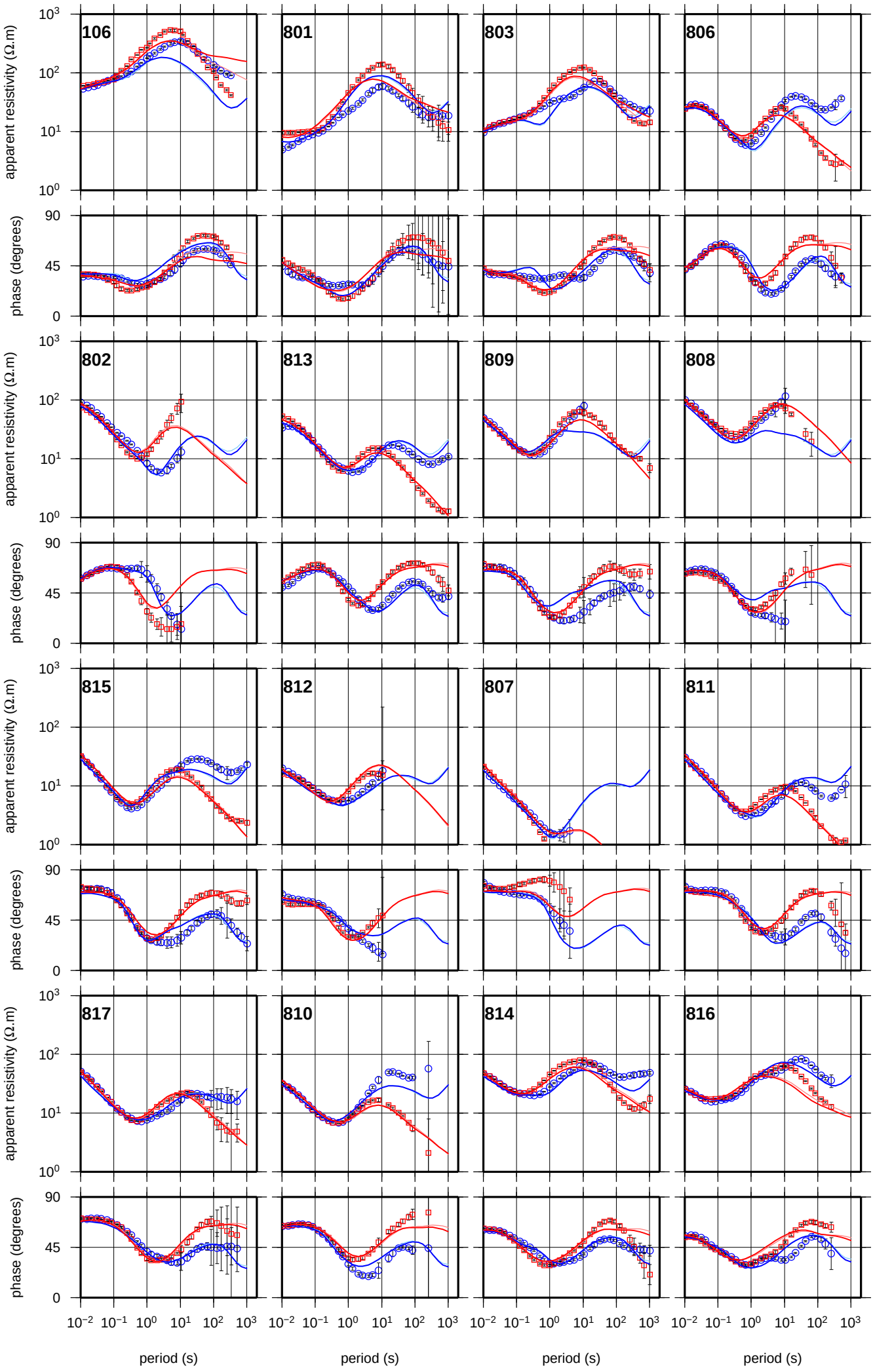
106
801
803
806
802
813
809
808
815
812
807
811
817
810
814
816
apparent resistivity (Ω.m)
phase (degrees)
period (s)

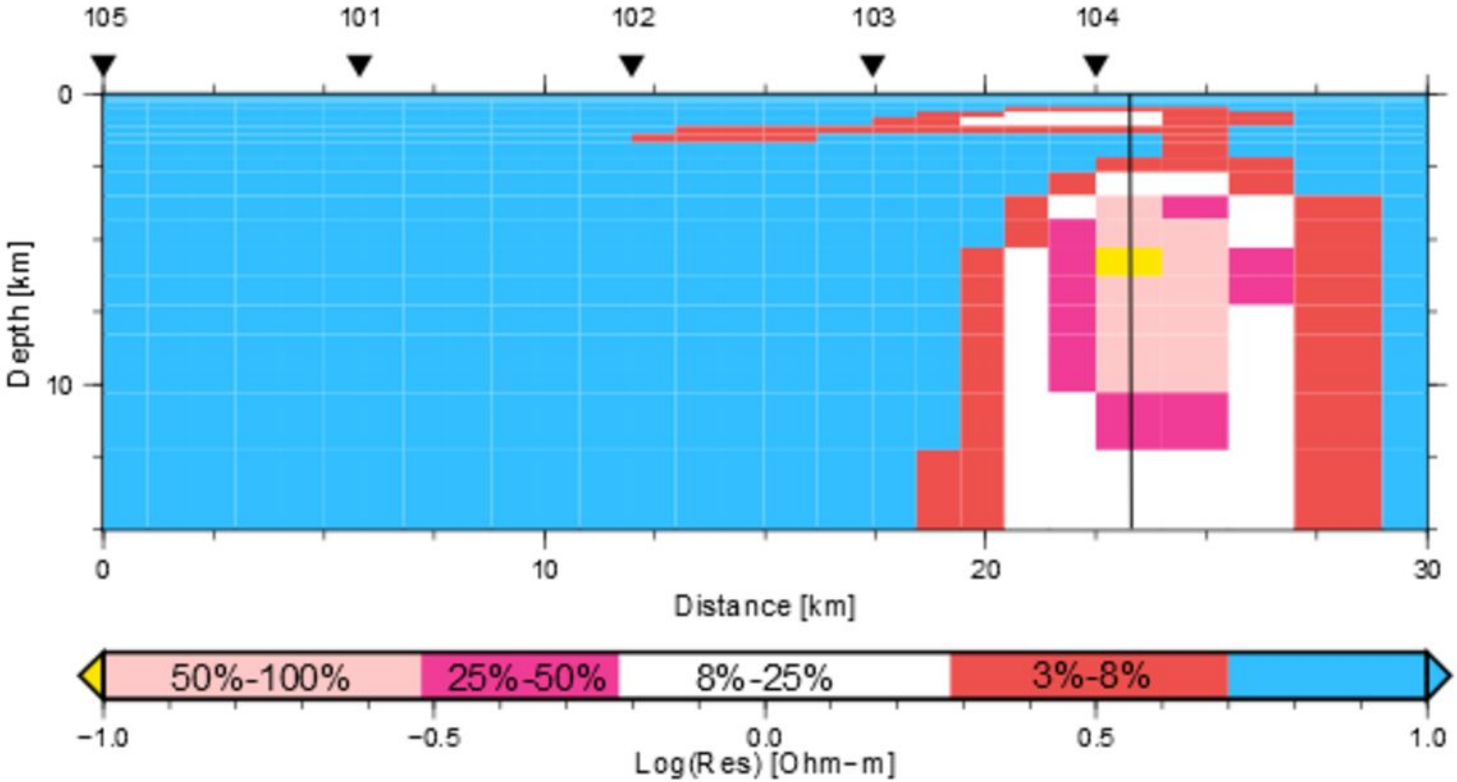
105
101
102
103
104
0
10
Depth [km]
0
10
20
30
Distance [km]
50%-100%
25%-50%
8%-25%
3%-8%
−1.0
−0.5
0.0
0.5
1.0
Log(Res) [Ohm−m]

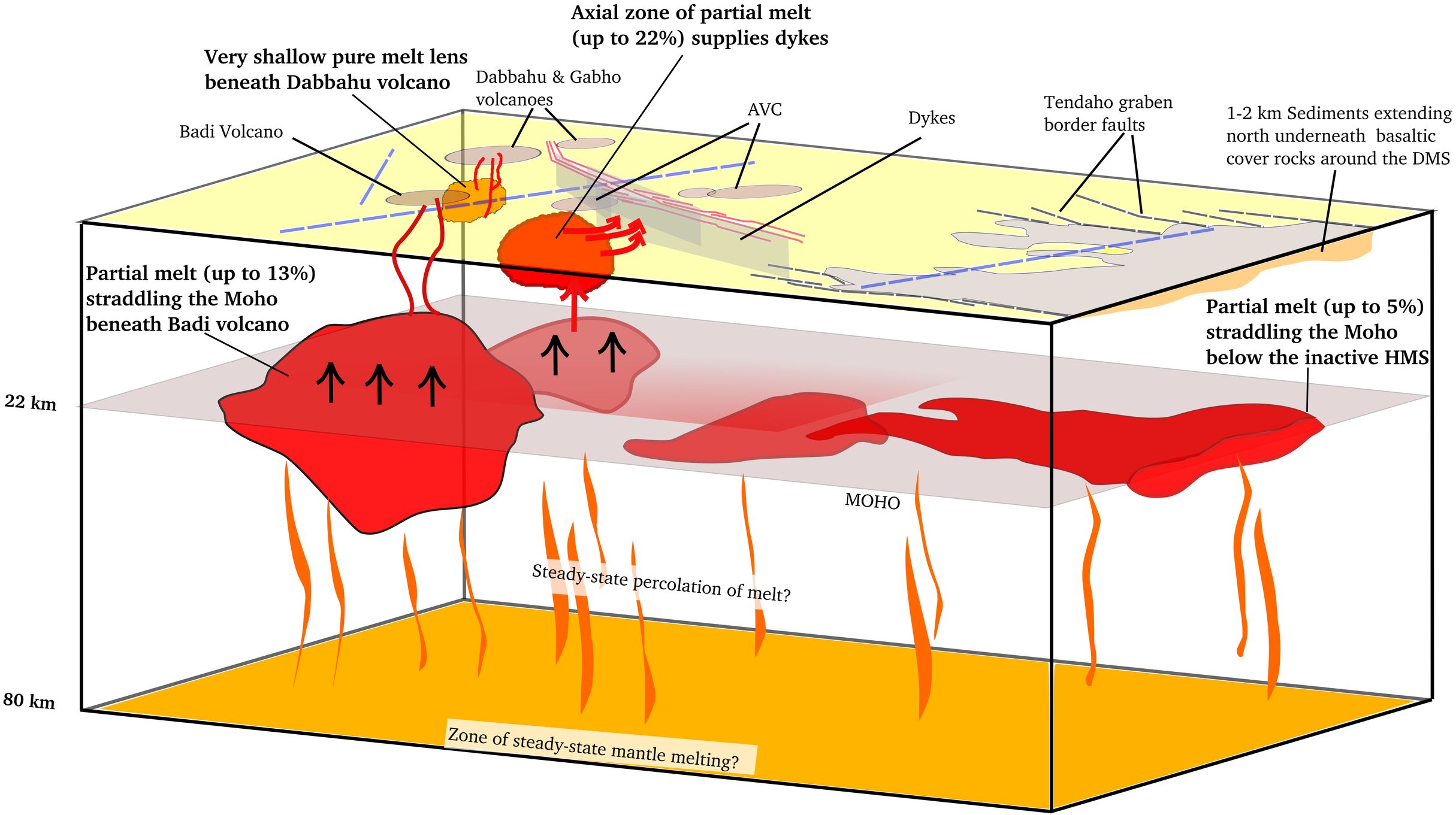
Axial zone of partial melt
(up to 22%) supplies dykes
Very shallow pure melt lens
beneath Dabbahu volcano
Dabbahu & Gabho
volcanoes
Badi Volcano
AVC
Dykes
Tendaho graben
border faults
1-2 km Sediments extending
north underneath basaltic
cover rocks around the DMS
Partial melt (up to 13%)
straddling the Moho
beneath Badi volcano
Partial melt (up to 5%)
straddling the Moho
below the inactive HMS
22 km
MOHO
Steady-state percolation of melt?
80 km
Zone of steady-state mantle melting?

Site	906	905	904	903	907	110	913	914	909	
Misfit		0.8	0.6	1.1	1.3	1.4	1.2	1.2	1.4	1.8
Site	910	911	908	912	915	916	917	Overall		
Misfit		0.7	1.2	1.4	1.4	0.8	1	1.5	1.2	

Site	105	104	103	102	101	Overall	
Misfit		1.4	1.9	1.7	1.4	1.3	1.6